Multiwall Carbon Nanotube Josephson Junctions with Niobium Contacts

Dissertation

zur Erlangung des Doktorgrades der Naturwissenschaften

(Dr. rer. nat.)

der naturwissenschaftlichen Fakultät II - Physik

der Universität Regensburg

vorgelegt von

Emiliano Pallecchi

aus Florenz

Februar 2009

Die Arbeit wurde von Prof. Dr. Ch. Strunk angeleitet.
Das Promotionsgesuch wurde am ... eingereicht.
Das Kolloquium fand am 17.02.2009 statt.

Prüfungsausschuss:	Vorsitzender:	Prof. Dr. Sergey Ganichev
	1. Gutachter:	Prof. Dr. Christoph Strunk
	2. Gutachter:	Prof. Dr. Milena Grifoni
	weiterer Prüfer:	Prof. Dr. Jascha Repp

Alla mia famiglia

Contents

Introduction

The two characteristic fingerprints of superconductivity are the flow of dissipationless supercurrent and perfect diamagnetism. In 1962 Josephson predicted that a supercurrent would also flow between two superconductors separated by a thin insulating barrier. This effect was observed in 1963 in tunnel junctions. After this first experiment many different types of "weak links" have been used as a bridge between two superconducting electrodes. In more recent years proximity induced supercurrent through individual carbon nanotubes has been observed. A carbon nanotube is a large molecule formed by one or more graphene sheets rolled up into a cylinder. A great variety of mesoscopic phenomena has been studied in carbon nanotubes and the observation of supercurrent through this molecule opens the possibility to study the interplay between mesoscopic physics and superconductivity. The experimental observation of a dissipationless supercurrent in gated carbon nanotube remains challenging because of the extreme sensitivity of the junctions to the environment and to noise fluctuations. In single wall nanotubes a supercurrent is measured when a broad degenerate level is in resonance with the contacts. The results are qualitatively in agreement with the theory recently developed by van Houten and Beenakker but the values of the measured critical currents are much smaller than what theory predicts. For multiwall carbon nanotubes the situation is less clear. In molecular junctions the critical currents are typically several orders of magnitude lower than what observed in more conventional Josephson junctions so that thermal fluctuations are not negligible even at the lowest temperature reached in experiments. A higher supercurrent would be desirable to allow a more thorough study of the proximity induced superconductivity in molecular conductors and for new devices such as the nanosquid.

We address these issues by choosing niobium as a superconductor and by designing an optimized on chip electromagnetic environment. The main goal of this thesis is the investigation of dissipationless supercurrent in multiwall carbon nanotubes embedded in a controlled environment. The environment is meant to reduce the suppression of the supercurrent and allows to disentangle the effects of thermal fluctuations from the

intrinsic behavior of the junction. This is crucial for the extraction of the value critical current from the measured data.
At positive gate voltage the contacts transparency is lowered and Coulomb blockade is observed. This allows to use Coulomb blockade measurements to further characterize the nanotube and to study the physics of a quantum dot coupled to superconducting leads. The last part of this thesis is dedicated to the measurements of a carbon nanotube Josephson junctions in the Coulomb blockade regime.
The thesis is organized as follows: in the first chapter we briefly review the basic electronic properties of carbon nanotubes. First we introduce the peculiar band structure that nanotubes inherit from graphene, then we discuss some of the main relevant effects observed in transport experiments with MWNTs. In the second chapter we introduce the Josephson effect and we describe the extended resistively and capacitively shunted junction model (RCSJ). In Chapter 3 we illustrate the sample preparation and the measurement schemes that we used. In Chapter 4 we discuss the measurements of our Nb/MWNT/Nb junctions. First we present a characterization of the junction and then we report on the gate dependence of the supercurrent. Finally we use the extended RCSJ model to analyze the experimental data. Chapter 5 is dedicated to measurements in the Coulomb blockade. We first present a study of the distribution of the peak spacing and then we discuss the stability diagram measured in zero and high magnetic field.

Chapter 1

Electronic Properties of Carbon Nanotubes

In the first part of this chapter we introduce the band structure of graphene and then derive that of carbon nanotubes by imposing periodic boundary conditions. In the second part we will briefly review the different transport regimes typically observed in experiments. The last section is dedicated to Coulomb blockade, that will also be the focus of Chapter 5 where the measurements in this regime are presented. This chapter is mainly based on the book of Saito et al. [1] and on the review of Roche et al. [2]. For the Coulomb blockade section we follow Ref. [3, 4]

1.1 Band structure of Carbon Nanotubes

1.1.1 Graphene

Graphene is a planar sheet formed by carbon atoms arranged in an hexagonal lattice with an sp^2 hybridization. The $2s, 2p_x, 2p_y$ orbitals form in-plane σ-bonds and determine the mechanical properties of graphene. The energies associated to the σ bands are far away from the Fermi energy, therefore they do not usually contribute to the transport properties. The p_z atomic orbitals, perpendicular to the graphene plane, do not overlap with the other orbitals and hybridize to form a π (bonding and antibonding) delocalized band. The structure of the π band of graphene can be calculated analytically in the tight-binding model and the nearest neighbours approximation.

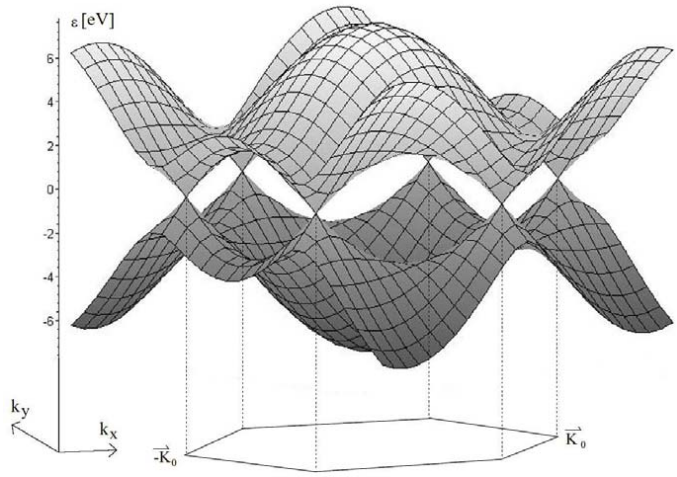

Figure 1.1: The band structure of graphene. The valence and the conductance bands touch at the six corners of the first Brillouin zone.

The resulting dispersion relation is given by:

$$E(k_x, k_y) = \pm t \left\{ 1 + 4\cos\left(\frac{\sqrt{3}k_x a}{2}\right)\cos\left(\frac{k_y a}{2}\right) + \cos^2\left(\frac{k_y a}{2}\right) \right\} \qquad (1.1)$$

where t is chosen -3.033 eV to reproduce first principles calculations and $a = 2.56$ Å is the lattice constant. The band structure is plotted in Fig.1.1.The valence and the conduction bands touch at the six corners of the first Brillouin zone, therefore graphene behaves like a zero gap semiconductor.

1.1.2 Zone Folding

A single wall carbon nanotube (SWNT) can be obtained by rolling up a graphene sheet. A vector connecting to sites A and A' of the graphene lattice is called *chiral vector* C_h and can be fully defined by a pair (n, m) such that

$$\mathbf{C_h} = n\mathbf{a_1} + m\mathbf{a_2}, \qquad (1.2)$$

with $\mathbf{a_1}$ and $\mathbf{a_2}$ the basis vectors of the lattice. The geometrical structure of a carbon nanotube can be represented by the indices (n, m) corresponding to the chiral vector that connects two points on the graphene lattice that coincide once the nanotube is

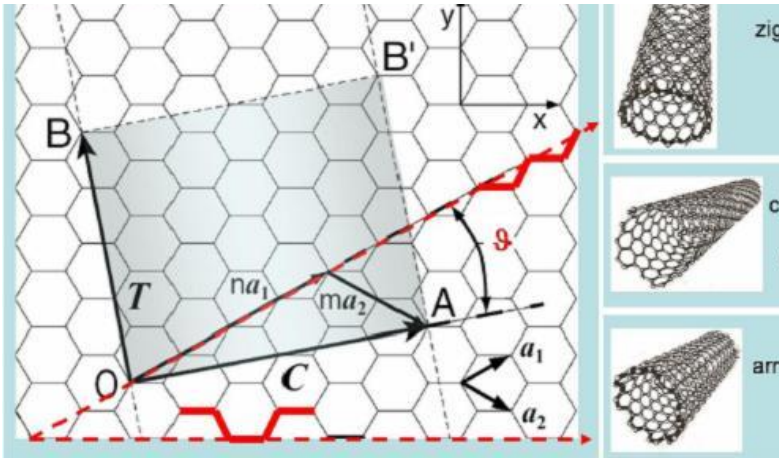

Figure 1.2: Zone folding of a graphene sheet. On the rigth an armchair, a zigzag and a chiral tube are shown.

rolled up, Fig. 1.2. A carbon nanotube is called *armchair* if $n = m$, *zigzag* if $m = 0$ and *chiral* otherwise. The name reflects the shape of the cross-section of the tube.
Multiwall carbon nanotubes (MWNTs) are formed of concentric single wall nanotube shells, each shell inside the next one. The interlayer distance in multiwall nanotubes is close to the distance between graphene layers in graphite, approximately 3.3 Å.
The band structure of an infinitely long SWNT can be derived from that of graphene by imposing boundary conditions along the circumference. Only certain $\mathbf{k}$ vectors perpendicular to the tube axis are allowed, leading to the formation of one-dimensional subbands. The allowed $\mathbf{k}$ vectors perpendicular to the tube axis are those satisfying a periodical boundary condition around the circumference:

$$k_\perp = \pm \frac{2n\pi}{C} \tag{1.3}$$

where $k_\perp$ is the modulus of the vector, C denotes the circumference of the nanotube, and n is an integer number. From this quantization it results that a carbon nanotube is metallic or semiconducting depending on whether the subbands include the K and K' points or not. The band structure is fully determined by the geometry and can be related to the chiral indices (n, m): armchair nanotubes are always metallic; zigzag and chiral tubes are metallic only if $(2n + m)$ is a multiple of 3. For metallic tubes the dispersion relation is linear at the Fermi energy where two two-fold degenerate one dimensional subbands cross. For semiconducting a gap opens at the Fermi energy,

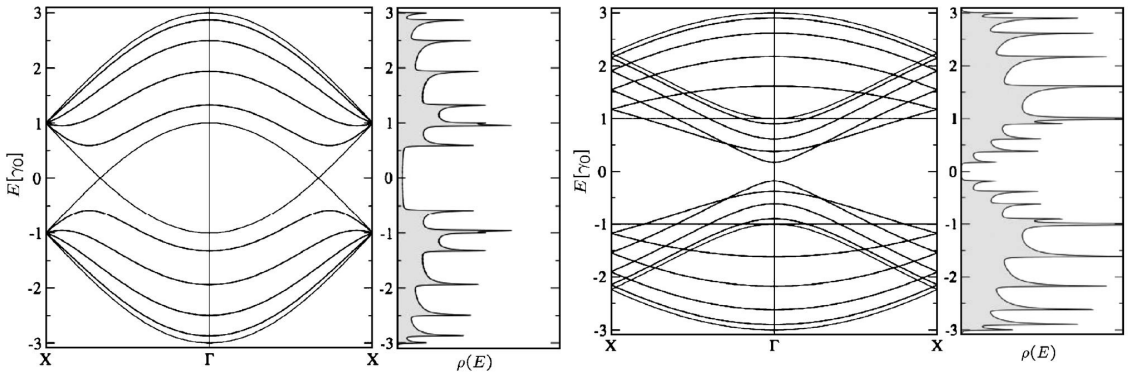

Figure 1.3: Band structure and density of states (left image) of an armchair nanotube (5,5), and a semiconducting zigzag tube (7, 0) (shown on the right image). Source: Ref. [2]].

as sketched in Fig. 1.3.

1.1.3 Role of Disorder

There are several types of disorders that can be present in carbon nanotubes, mainly classified as structural defects and adsorbates. Structural defects refer to the fact that the nanotube lattice differs from the perfect hexagonal one, for instance because of one carbon atom is missing (*vacancy*) or is not at the right position (*dislocation*). A second type of structural defect is the atomic substitution, which consists of having a carbon atom of the lattice replaced by an atom of a different kind. The adsorbates are impurities located on the surface of the nanotube. They can be catalytic nanoparticles involved in the growth process, a result of the sample fabrication, or molecules adsorbed from air. Ando et al. [5] showed that for metallic nanotubes and long-range, slowly varying potential impurities, the low energy back scattering is suppressed. For semiconducting tubes the scattering is found to be much stronger. A convenient way to address the more general case of disordered nanotubes is to look a the elastic mean free path. An analytic expression can be derived for the elastic mean free path for an energy close to the charge neutrality point and on-site Anderson-type disorder:

$$L_{el} = \frac{18 a_{cc} \gamma_0}{W^2} \sqrt{n^2 + m^2 + nm}, \tag{1.4}$$

where a_{cc} is the distance between two carbon atoms in the graphene lattice, γ_0 is 2.9 eV, and W is the strength of the disorder. From equation 1.4 follows that the elastic mean free path is proportional to the diameter and scales with the square of the disorder strength. Numerical studies [2] confirm this dependence and show that the elastic mean free path is further reduced for energies corresponding to an higher density of states.
Multiwall carbon nanotubes are a more complicated system due to the presence of many shells. Experiments on multiwall nanotubes [6] suggest that thinner tubes are less diffusive, probably due to better growth conditions. In most cases different shells are incommensurate, and it is not possible to find a unit cell for the system. It has been shown that for infinitely long and clean intra-shell incommensurate nanotubes the tunneling is zero. However, for finite length tubes at high bias or temperature the intershell coupling increases and more than one shell can participate in transport [7]. The aperiodic random potential of the inner shells causes a reduction of the elastic mean free path even in absence of intershell coupling, resulting in a crossover from quasi ballistic to diffusive transport, even for defect-free carbon nanotubes [8].

1.2 Transport Properties of Carbon Nanotubes

The transport across an individual carbon nanotube connected to electrical reservoirs is extremely rich. It can be ballistic or diffusive, depending on the quality of the nanotube. While it is generally one dimensional for SWNTs, it is usually two dimensional (or quasi 1D) for MWNTs. The possibility to grow defect-free single wall carbon nanotubes makes them an ideal system to study one dimensional phenomena [9, 10, 11, 12, 13].
Clean SWNTs are ballistic conductors and the linear transport can be described within the framework of Landauer-Büttiker. The predicted two terminal conductance is given by:

$$G = \frac{2e^2}{h} \sum_i |T_i|^2 \tag{1.5}$$

where the sum is performed over all the channels and T_i is the transmission coefficient of the channel i. An undoped, defect free, single wall carbon nanotube has two two-fold degenerate channels at the Fermi energy, and the corresponding two point resistance is $(4 \cdot e^2/h)^{-1} = 6.5\,\mathrm{k}\Omega$. This four fold symmetry is due to spin and orbital degeneracy (corresponding to spin up and spin down electrons and electrons propagating clockwise and counterclockwise along the tube axis). Scattering events at the contacts or inside the tube can lead to an increase of the resistance.

For disordered nanotubes with an elastic mean free path that is shorter than the sample, the transport is not ballistic anymore. The conductance can be expressed in terms of sample length L, elastic mean free path L_{el}, and number of channels M [14]:

$$G \approx \frac{2e^2}{h} M \frac{L_{el}}{L + L_{el}}. \tag{1.6}$$

Depending on the temperature and on the transparency of the contacts, many different transport regimes and low dimensional phenomena can be studied in low temperature transport across individual carbon nanotubes: part of the popularity of carbon nanotubes within the condensed matter community is due to this. It is beyond the scope of this chapter to present all of them; in the rest of the chapter we will briefly review those which are the most relevant for the measurements presented in the Chapter 4 and 5.

1.3 Coherent transport

Carbon nanotubes are coherent conductors with a long phase coherence length at low temperature and therefore a good system to study quantum interference effects in low dimensional system. A typical example of the effect of quantum interference can be seen in the length dependence of the resistance of a long coherent diffusive conductor. When increasing the length L the resistance increases exponentially: the system becomes insulating, the electron wave functions near the Fermi energy are localized so that the probability for one electron to be transmitted from one electrode to the other goes to zero. Localization effects become important when the shorter between L and L_ϕ is smaller than L_C. The localization length L_C can be expressed as $L_C = ML_{el}$ [14], with M the number of modes of the conductor. We distinguish between two different types of localization: if $L_C < L_\phi$ the system is in the 'strong localization regime' while if $L_C > L_\phi$ we speak about 'weak localization'. In the strong localization regime the electrons are localized on a length scale of the order of L_C and the transport is given by thermally activated electron hopping between localized regions. In the 'weak localization' the phase coherence introduces an upper boundary to the size of the localized areas. The consequences of weak localization for charge transport will be analyzed in the next section.

1.3.1 Weak Localization

Let's consider a phase coherent conductor. The weak localization theory can then be well understood in terms of path integrals. The probability $P(r, r'; t)$ for one electron to go from a point $\mathbf{r}$ to $\mathbf{r}'$ is given by the modulus square of the sum of the amplitude probabilities $A(r, r'; t)$ for all the possible paths that join $\mathbf{r}$ and $\mathbf{r}'$. If the Fermi wave length of the electrons is shorter than their elastic mean free path and phase coherence length we can avoid a full quantum description of the system for a semiclassical one. This corresponds to restricting the summation to all the classical paths:

$$P(\mathbf{r}, \mathbf{r}'; t) = \left|\Sigma A_i\right|^2 = \Sigma |A_i|^2 + \Sigma_{i!=j} A_j^* A_i. \tag{1.7}$$

The total probability can be divided in two terms: the first is given by the sum of the probabilities along the different paths and it is the classical probability, the second term is a quantum correction due to the interference of different paths. This interference contribution averages out if the phase difference between different trajectories is uncorrelated, which is usually the case if $\mathbf{r} \neq \mathbf{r}'$. Let's consider now the special case $\mathbf{r} = \mathbf{r}'$, which obviously describes a backscattering event. For this special boundary condition the time reversed trajectories are always interfering constructively, leading to an enhancement of the backscattering. When quantum interference effects are taken into account we find this interference enhanced backscattering reducing the conductance by $2e^2/h$ with respect to the classical value. A unique signature of weak localization can be seen in the negative magnetoconductance. Applying a magnetic field perpendicular to the sample breaks the time reversal symmetry and suppresses the coherent backscattering. The magnetoconductance for a quasi 1D sample[15] is given by:

$$\Delta_{WL} = -\frac{e^2}{\pi \hbar L} \left(\frac{1}{L_\phi^2} + \frac{W^2}{3 l_m^4} \right)^{-1/2} \tag{1.8}$$

with W the width of the sample, B the applied magnetic field, and $l_m = (\hbar/eB)^{1/2}$ is the magnetic length. From equation 1.8 follows that the magnetoconductance measurements in the weak localization regime can be used for the determination of the phase coherence length since all the other parameters are usually known in experiments.

1.3.2 Universal Conductance Fluctuations

The conductance of a set of samples in the diffusive regime varies from sample to sample. Classically these fluctuations are negligible. When the size of the sample approaches the

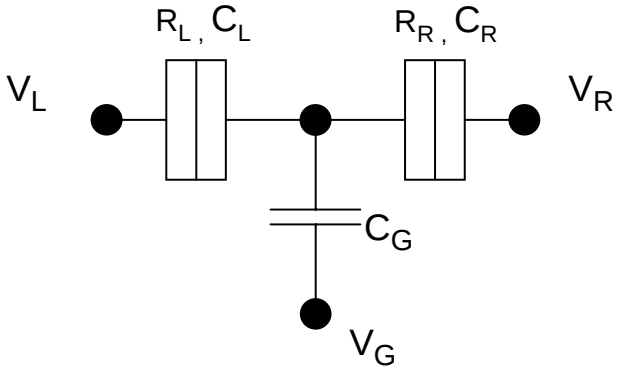

Figure 1.4: Schematic view of a single electron transistor. R_L and R_R represent the tunnel resistances of the left and right contacts, C_L and C_R the contact capacitances and C_G the gate capacitance, V_L, V_R, and V_G are the voltage applied to the contacts and the gate respectively.

phase coherence length we cannot neglect quantum interference effects anymore. These effects are responsible for large sample to sample fluctuations. The amplitude of the fluctuations for a fully coherent sample is $\delta G \approx e^2/h$ for $T = 0$ regardless of its size, shape, or resistivity of the sample; for this reason they are called *Universal Conductance Fluctuations*. When the sample length L is larger than L_ϕ the sample is divided in L/L_ϕ coherent segments which fluctuate independently. As a result the fluctuations are reduced to a smaller value[16]:

$$\delta G = 2\sqrt{3}\frac{2e^2}{\hbar}\left(\frac{L_\phi}{L}\right)^{3/2} \tag{1.9}$$

At finite temperature a smearing of the conductance fluctuations is expected if the thermal length $L_T = \sqrt{\hbar D/k_B T}$ exceeds the coherence length L_ϕ.

1.4 Coulomb blockade

A metallic island connected to two leads by tunnel junctions and capacitively coupled to a gate (scketched in Fig. 1.4) is referred to as a single electron transistor (SET).
The energy that has to be paid to add one extra electron to the island is of the order of the *charging energy* $E_C = e^2/C_\Sigma$, with $C_\Sigma = C_L + C_R + C_G$ the sum of the

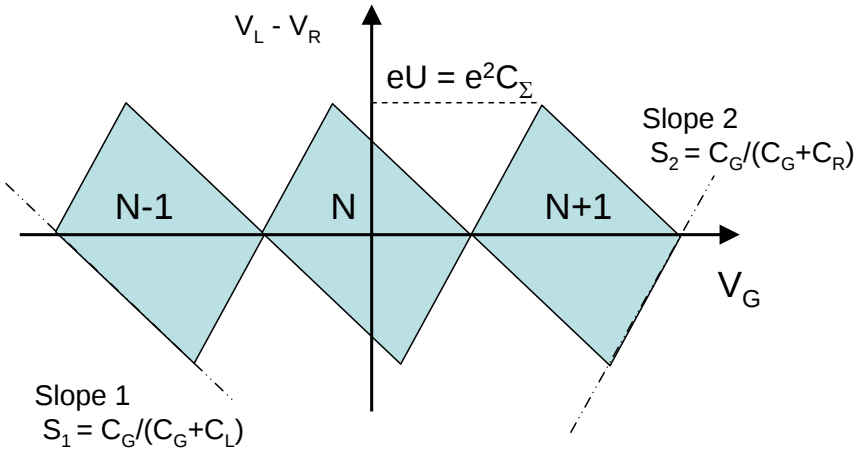

Figure 1.5: The blue diamonds describe the regions of the stability diagram where the number of charges on the island is fixed. The slope of the diamonds and the their heights are related to the capacitances via the formulas shown in the figure.

capacitances between the island and the leads and between the island and the gate. When the geometrical sizes of the system are in the nanometer range, typical values of the capacitances can be extremely low, of the order of $1 - 100$ aF. One of the most spectacular consequences of this ultra low capacitance appears at low temperature, when

$$k_B T \ll e^2/2C_\Sigma. \tag{1.10}$$

Typical values of E_C for carbon nanotubes are in the milli-electronvolt range. This corresponds to a temperature $T = E_C/k_B \approx 10$ K that is much higher than those reached with cryogenic a refrigerator, so that this regime is accessible experimentally. When the condition presented in Eq. 1.10 is fulfilled, thermal fluctuations are not strong enough to change the number of charges on the island and, at least for low bias voltages, the transport is blocked. This phenomenon for which the tunneling of electrons is inhibited by Coulomb interactions is called Coulomb blockade.

A simple analysis based on electrostatics can be used to highlight some of the basic features of Coulomb blockade. In this picture the resistances R_L and R_R do not play any role and also thermal fluctuations are neglected. Tunneling from the gate is not allowed.

The equilibrium charge on the tube is given by the (integer) number of the electrons N_0 and because of charge conservation is related to the (continuous) charge on the

capacitors:[1]

$$Q_0 = -N_0 e = -(Q_L + Q_R + Q_G) = C_L V_L + C_R V_R + C_G V_G, \tag{1.11}$$

The free energy of the system $E_{Free} = E - UQ$ is composed of three terms: E_S is the electrostatic energy of the island, W is the work done by the batteries, and W' is the energy of the electrodes:

$$E_{Free}(N; V_L, V_R, V_G) = E_S - W - W'. \tag{1.12}$$

An analytic expression for E_{Free} can be obtained if the capacitances characterizing the system are known (see for instance Ref. SETphd. Such an expression allows to calculate the change in the free energy $\Delta E^{L/R}_{Free\,+/-}$ corresponding to a tunnel event from the left (right) electrode to the island (from the island to the electrode) for a fixed choice of the applied voltages. The total energy is a function of the charge Ne and the external potential V_L, V_R and V_G. We can therefore check for which values of parameters a state with a fixed N is stable against tunneling. This happens when all the four ΔE_{Free} that corresponds to changing the charge on the island by one are positive. In this case to change N is energetically disfavored with respect to keeping it fixed. Inside the area in the parameter space that corresponds to a fixed N the current is not allowed to flow through the island. This area forms a characteristic diamond pattern in the plot of the differential conductance versus gate and bias voltage (Fig. 1.5). Moving from one diamond to the next one implies to change N by one. From such a diagram, also called *stability diagram*, it is possible to extract the electrostatic parameters characterizing the sample: the diamond height is $eV_{max} = e/C_\Sigma$, while the capacitances can be extracted from the slope of the diamonds. The diamond allows also to determine the so called 'lever arm' α which translates a change in gate voltage to the corresponding energy shift:

$$\alpha = E_C/\Delta V_G = C_G/C_\Sigma \tag{1.13}$$

Coulomb blockade measurements are a very powerful tool for accurate measurements of very low capacitances and the determination of the charge state.

1.4.1 Master Equation Description

The electric current flowing through a single electron transistor can be obtained using a master equation approximation. We will consider the simple case of a metallic dot

[1] for simplicity we neglect the charge background

where the density of states can be considered as a continuum, but this approach can be extended to the case of discrete states.
The rate for changing the electron number on the island from $N \rightarrow N+1$ tunneling from the left electrode, according to the Fermi golden rule and assuming a Fermi distribution $f(\epsilon)$ for both leads and island, is given by [4]:

$$\Gamma^{L}_{N\rightarrow N+1} = \frac{1}{e^2 R_L}\int d\epsilon_L \int d\epsilon_{island} f_L(\epsilon_L)(1-f_{island}(\epsilon_{island}))\delta(\Delta E_L + \epsilon_L - \epsilon_{island}) \tag{1.14}$$

where ϵ_L is the energy of the left reservoir and

$$\Delta_{L/R}(n) = \frac{e^2}{C_\Sigma}(N - N_0 + 1/2) + eV_{L/R} \tag{1.15}$$

is the total energy change corresponding to a tunneling of one electron from the left/right contact to the island. Eq.1.14 can be integrated using the relation $\int d\epsilon f(\epsilon)(1-f(\epsilon - E)) = E\exp(E/k_B) - 1)$, one then find:

$$\Gamma^{L/R}_{n\rightarrow n+1} = \frac{1}{e^2 R_{L/R}} \frac{\Delta E_{L/R}(n)}{\exp(\Delta_{L/R}(n)/k_b T)} - 1 \tag{1.16}$$

In a similar way it is possible to find the rate for all the possible processes that change the number of electrons on the island by one. We restrict ourselves to consider only sequential tunneling, this approximation is valid for high tunnel resistances $R_{L/R} \gg R_K$, with $R_K \approx 25.8\,\mathrm{k}\Omega$.
For practical reasons we define $\Gamma_{i\rightarrow j} = \Gamma^{L}_{i\rightarrow j} + \Gamma^{R}{}_{i} \rightarrow j$. We can now write the master equation for the system:

$$\frac{dp_N}{dt} = \Gamma_{N+1\rightarrow N}p_{N+1} + \Gamma_{N-1\rightarrow N}p_{N-1} - (\Gamma_{N\rightarrow N+1} + \Gamma_{N\rightarrow N+1})p_N. \tag{1.17}$$

To find a steady state solution we now have to require that the probabilities do not change with time, and this can be achieved by imposing that the different contributions on the right hand side of Eq.1.17 cancel out. This condition is called $detailed\ balance$ and it reads:

$$\Gamma_{N\rightarrow N+1}p_N = \Gamma_{N+1\rightarrow N}p_{N+1} \tag{1.18}$$

The probability can be easily computed by setting an initial condition, using recursively Eq. 1.18 and imposing the normalization $p_n \rightarrow p_n/\Sigma p_n$. The current is related to the

probability by:

$$I = -e \sum_N p_N (\Gamma^L_{N \to N+1} - \Gamma^L_{N \to N-1}). \tag{1.19}$$

In Fig. 1.6 we plot the linear conductance as a function of gate voltage and temperature. The shape of this curve is characteristic of Coulomb blockade: the conductance at zero bias is mainly zero, corresponding to a fixed number of electrons inside the dot, but, in correspondence of a peak where the energies of two configurations with N and $N \pm 1$ electrons on the island are degenerate, the current is allowed to flow. The conductance is extremely sensitive to a small change of the charge on the gate electrode, for this reason the SET is also used to fabricate charge detectors with a very high resolution. When the temperature is increased the Coulomb blockade is less pronounced and for $k_B T \approx E_C$ the Coulomb blockade is completely suppressed.

The color plot of the DC conductance and of the differential conductance as a function of bias and gate voltage is shown in Fig. 1.6, the parameters have been chosen to mimic ones of the measured samples. The diamond pattern expected from the electrostatic model is clearly visible in the stability diagram. In case of a metallic island the spacing between the peaks ΔV_G is directly related to the gate capacitance $\Delta V_G = e/C_G$ while the width of the peak is determined by the temperature T and by the rate Γ.

When the size of the island is such that its density of states is discrete the Coulomb blockade is modified with respect to the case of a metallic island with continuous density of states. In this case we call it a quantum dot and then the energy that has to be paid to add an extra electron (the addition energy) is given by the sum of the charging energy and level spacing. In clean single wall carbon nanotubes each level is 4 fold degenerate (2 for spin and 2 for orbital degeneracy) and therefore the diamond pattern is formed by 3 small and one bigger diamond. The first three diamonds correspond to adding three electrons to the same level where a first electron is situated. The addition energy is in this case equal to the charging energy and the situation is analogous to the case of a metallic island. To add a fourth electron to the same level is not possible so that the energy that has to be paid is given by the sum of the energy necessary to reach the next level, the level spacing δE, plus the charging energy E_C.

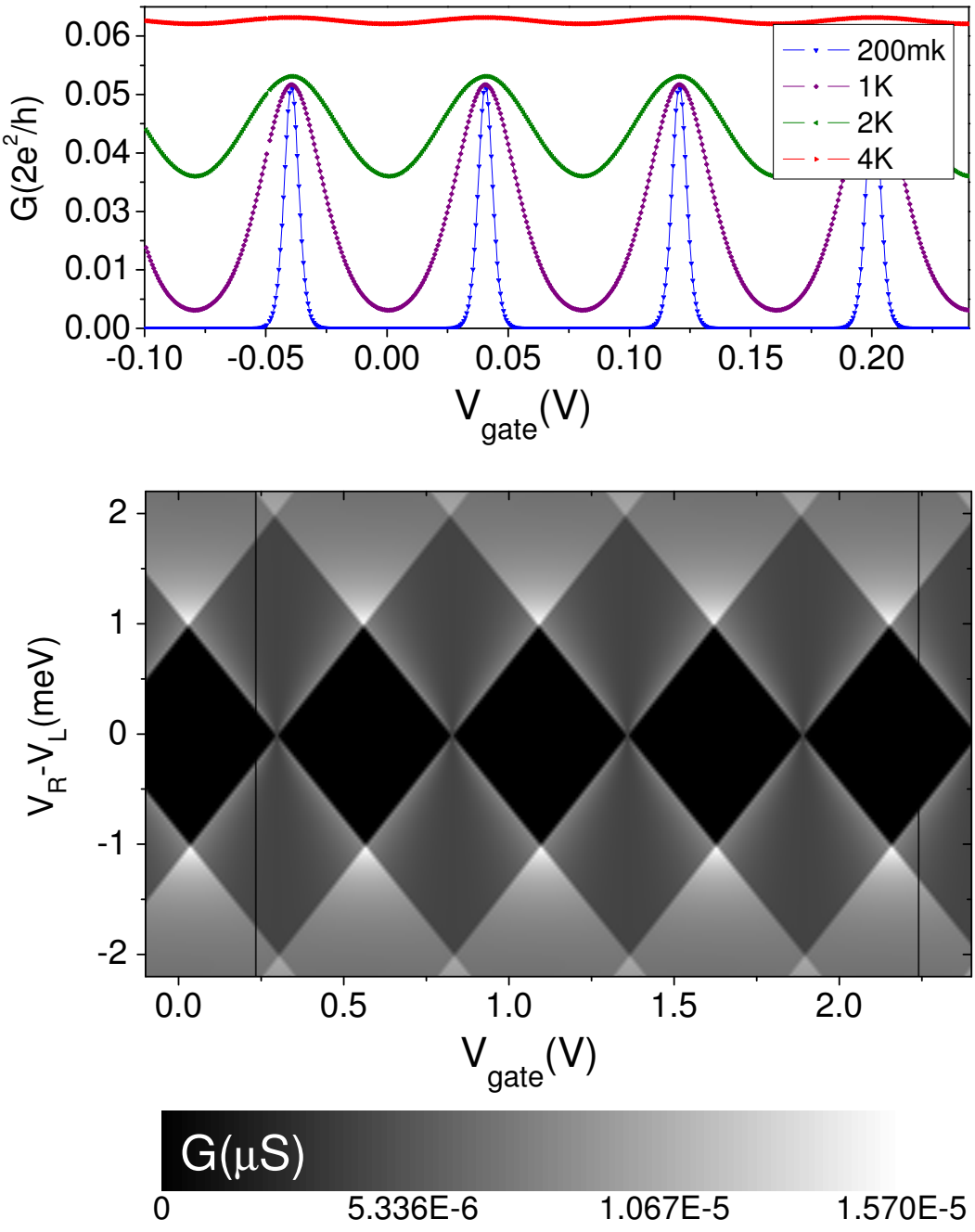

Figure 1.6: (a) Linear conductance as function of gate voltage and temperature. For a metallic island the Coulomb peaks are equally spaced and are directly related to the gate capacitance. (b) Stability diagram obtained within the model described in the text. The gray scale represents the differential conductance dI/dV. The Junction parameter for both graph are similar to that observed in the experiments: $R_L = R_R$ = 60 kΩhm, $C_L = C_R = 50\,aF, C_G = 2aF$.

Chapter 2

Proximity induced superconductivity

Superconductivity is an exciting field and after almost a century from its start it is still very active. In this chapter we will concentrate on the Josephson effect, while we will not discuss BCS theory in detail since it is now a well established theory and it has been the focus of several excellent books [17, 18]. After a brief introduction to the Josephson effect, we present the model we will use to analyze the measurements presented in Chapter 4. First we consider a simplified model for the junction dynamics and then we extend it to include the effect of the environment and of thermal fluctuations. The model is based on the work of Martinis and Kautz [19, 20]. We will show that these effects play a major role in particular in small critical current Josephson junctions, as it is the case for carbon nanotube weak links.

2.1 Superconductivity

In 1911, three years after liquefying helium, Heike Kamerlingh Onnes observed that the resistance of mercury vanishes below a certain critical temperature T_c [21]. The first satisfactory microscopic theory of superconductivity, the Bardeen-Cooper-Schrieffer theory (or BCS), appeared more than forty years later, following the discovery of Cooper which proved that the electron Fermi sea is unstable against the formation of pairs of electrons with opposite momentum and spin if an attractive interaction is present.[1] In the ground state of a BCS superconductor the electrons act in pairs and form a macroscopic

[1] In metals such an interaction results from the exchange of virtual phonons.

state. The BCS theory allows to calculate the properties of the ground state of the system and the quasi-particle excitation spectrum, which is given by:

$$E_k = \sqrt{(E_k - E_F)^2 + \Delta^2} \ . \tag{2.1}$$

The lowest excitations are located at energy 2Δ above the energy of the ground state, for this reason 2Δ is also called energy gap. The excitations are called Bogoliubov quasi-particles, differing in their dispersion relation from "normal" electrons.
In case of weak attractive interaction, as for normal metals, the order parameter is almost constant for $T/T_c \ll 1$ and goes to zero with a vertical tangent for T approaching T_c. in other words, the value of Δ is almost constant until the temperature is high enough for a relevant number of quasi-particle being excited.

2.2 Mesoscopic Josephson Effect

Between two superconductors separated by a thin insulating barrier a zero voltage supercurrent can flow [22]. This phenomenon is called the Josephson effect, from the name of the scientist who first predicted it. The supercurrent I is related to the phase difference φ of the Ginzburg-Landau wave functions of the superconductors by the following relationship:

$$I = I_c \sin\varphi \ . \tag{2.2}$$

An equation of the form of Eq. 2.2 where the current is related to the phase difference of the two superconducting wave functions is usually referred to as the $current \ \ phase \ \ relation$ or CPR. The maximum value of the supercurrent that can flow through the junction is called the $critical \ current \ I_c$ of the junction. The value of I_c depends on the superconductor, on the transparency of the tunnel barrier, and on the temperature. For tunnel junctions Josephson predicted $I_c = \pi\Delta/2eR_n$ with R_n the normal state resistance.
Moreover, when a voltage difference V is applied across the junction, the phase difference evolves with time according to the second Josephson equation:

$$d(\varphi)/dt = 2eV/\hbar \ . \tag{2.3}$$

From these two relations it follows immediately that a voltage V applied across the junction produces a sinusoidal current with amplitude I_c and frequency $\nu = 2eV/h$. This is also known as the $AC \ Josephson \ effect$ [23]. It is remarkable that the Josephson effect is a more general phenomenon that describes the physics of two superconductors

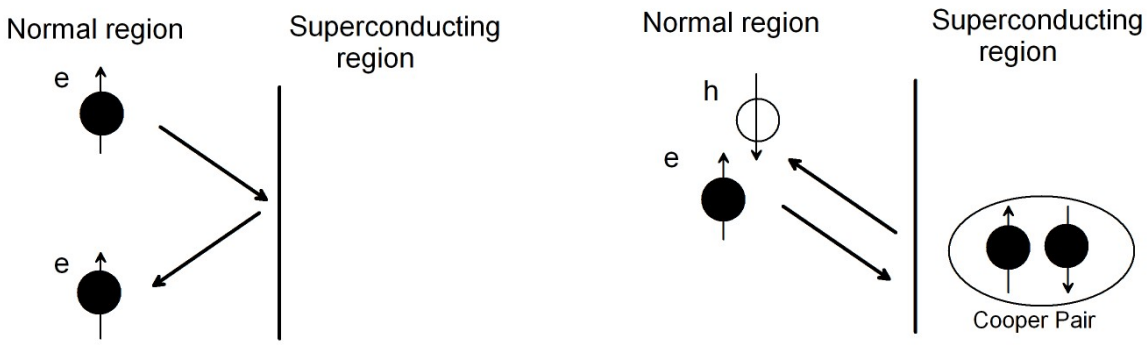

Figure 2.1: (a) Normal reflection at the N-S interface. (b) Andreev reflection, the electron is retro reflected as a hole and a Cooper pair is injected into the superconductor. The arrows indicate the momentum and the spin of the particles

connected by many kinds of *weak links* [24]. After pioneering experiments with a tunnel barrier also normal metals, ferromagnets, molecules and even individual atoms have been used as weak link [25].

Many efforts were made to calculate the current phase relation of Josephson junctions and the expected value of R_nI_c product. In the case of tunnel junction the value of R_nI_c is set by the superconducting gap of the electrodes:

$$R_nI_c(T=0) = \frac{\pi\Delta}{2e} \tag{2.4}$$

The calculation is more complicated when a metallic bridge of length L is used as a weak link. For short junctions ($L < \xi_S$ with L being the length of the junction and ξ_S the superconducting coherence length) it has been shown that in the ballistic and diffusive limit the value of the product R_nI_c is respectively 2 and 1.32 times that of a tunnel junction. For long junctions, the R_nI_c product is related to the Thouless energy E_{Th} rather than to the superconducting gap:

$$R_nI_c(T=0) = \frac{10.3}{e}E_{Th}. \tag{2.5}$$

A more modern view of the Josephson effect relies on the concept of Andreev bound states. This theory, if compared to the previous one, is much more general and can be applied to many different types of weak links.

The Andreev reflection can be best understood considering first a simple normal metal-superconductor junction. An electron coming from the normal region with energy $E < \Delta$

impinging on the interface cannot penetrate into the superconductor because of the gap in the density of states. The electron can either be normal reflected by reversing the component of the momentum perpendicular to the interface, or can form a pair with a second electron with opposite momentum and spin and then enter the superconductor as a Cooper pair. In other words, the electron is retro-reflected (or Andreev reflected) as a hole and a Cooper pair is injected into the superconductor, as depicted in Fig 2.1. It is important to stress the fact that the Andreev reflection is a phase coherent process: the retroreflected hole is phase shifted with respect to the electron by an amount that depends on the k vector of the electron and on the phase of the superconductor. For an ideal N-S interface with a perfect transparency $T = 1$ all the electrons with energy $E < \Delta$ are Andreev-reflected and since for every electron with energy above the Fermi level reaching the interface two electrons are transmitted, the conductance is twice that of the normal state. If the interface is not perfect and $T < 1$ part of the electrons are normal reflected and the conductance is reduced.

In a Superconductor - Normal metal - Superconductor (SNS) junction Andreev reflections occur at both interfaces. When one electron moving to the right reaches the interface it is Andreev reflected as hole and a Copper pair is injected into the right superconducting electrode. When the hole crosses the left S-N interface, it is Andreev reflected as an electron and a Cooper pair is removed from the right electrode. It can be shown by solving the so called Usadel equations for a single S-N interface that at each reflection the quasiparticle gains a phase shift that depends on k and on the phase of the superconductor. If the phase shift acquired during one complete cycle is $\delta = 2\pi n$ with $n = 1, 2, ..$ all the cycles interfere constructively and a localized Andreev bound states is formed. The Andreev bound states are responsible for the transfer of Copper pairs from one side of the junction to the other.

The transport properties of a mesoscopic conductor connected to two leads are determined by the set of the transmission probabilities $\{\tau_1, \tau_2, .., \tau_N\}$ of the N channels contributing to the transport. In systems such as the superconducting atomic point contact this set of transmission can be determined experimentally by fitting the non linear IV characteristic and used to characterize the junction itself. In the simple case of a short junction ($L < \xi_S$ with L the length of the junction and ξ_S the superconducting coherence length) in the clean limit ($\Delta \gg E_{Th}$ where E_{Th} is the Thouless energy), and a single conducting channel of transparency τ, two Andreev bound states are formed with energies:

$$E_{\pm}(\varphi, \tau) = \pm\Delta\sqrt{1 - \tau \sin^2(\varphi/2)}. \tag{2.6}$$

Each state carries a current in opposite direction according to the following equation:

$$I_{\pm} = \varphi_0 \frac{\partial E_{\pm}}{\partial \varphi} = \mp \frac{e\Delta}{2\hbar} \frac{\tau sin\varphi}{\sqrt{1 - \tau \sin^2(\varphi/2)}} \tag{2.7}$$

and the net supercurrent is given by the population imbalance of the two states.

$$I(\varphi, \tau) = \frac{e\tau\Delta}{2e\hbar} \frac{\tau sin\varphi}{\sqrt{1 - \tau \sin^2(\varphi/2)}} \tanh\left(\frac{E_+(\varphi, \tau)}{k_B T}\right). \tag{2.8}$$

In the limit of low transparencies, typical for tunnel junctions, the current phase relation is sinusoidal and the first Josephson equation is obtained.
The situation is more complicated when the junction is longer than the superconducting phase coherence length ξ_S, then Andreev bound states are formed. In the limit of $E_{Th} \gg \Delta$ the energy of the Andreev bound states is given by:

$$E_n^{\pm}(\varphi) = \frac{\xi_0 \Delta(T)}{L}[2\pi(n + 1/2) \mp \varphi]. \tag{2.9}$$

If the Thouless energy is smaller than Δ, then the Andreev spectrum is not discrete anymore and E_{Th} is the characteristic energy scale that sets the properties of the junctions, i.e. the value of the $R_n I_c$ product.

2.3 Temperature dependence

The temperature dependence of the critical current $I_c(T)$ has been calculated for different types of weak links [27, 28, 29, 26, 30] by several authors and analytically approximated expressions for several kinds of weak links have been found before the microscopic model based on the Andreev reflection presented in the previous section was developed. We should stress that if the set of transmissions τ of the sample is known it is possible to calculate $I_c(T)$ using Eq. 2.8. The result for a tunnel junction, for a short junction in the clean limit, and for a long junction are presented in Fig. 2.2.

2.4 The resistively and capacitively shunted model

We have seen in the previous section that if the parameters describing the transport through the weak link are known it is possible to predict the temperature dependence of the critical current. In reality, the behavior of a Josephson junction can be strongly influenced by the electromagnetic environment in which the junction itself is embedded

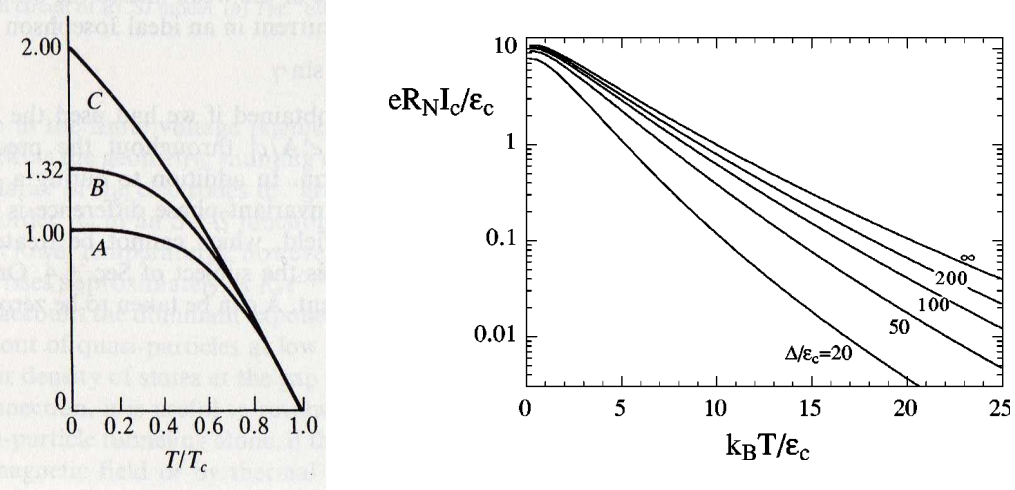

Figure 2.2: Temperature dependence for several kinds of Josephson junctions. Left: $I_c(T)$ for a tunnel junction (A) and for a metallic short junction in the clean (B) and dirty (C) limit (from ref. [17]. Right: temperature dependence of I_c for a long Josephson junction. The main energy scale is the Thouless energy E_{Th} and the different curves correspond to different value of at the ratio Δ/E_{Th}, adjusted from ref. [26]

and can differ substantially from the one of an ideal isolated junction. It is essential to include the environment in the model to correctly interpret the results of the measurements. The easiest model to describe a realistic Josephson junction is the resistively and capacitively shunted junction (RCSJ) model. The equivalent circuit used to model the junction is shown in Fig. 2.3. In the limit of a sinusoidal CPR, the equations describing the junctions are:

$$I = I_c \sin\varphi + \frac{V}{R} + C\frac{dV}{dt} \tag{2.10}$$

where I denotes the bias current, I_c the critical current of the junction, φ the phase difference, and R and C indicate the junction resistance and capacitance. It is convenient to express the voltage V in terms of the phase difference across the junction by using the second Josephson relation $d\varphi/dt = 2eV/\hbar$. Then the previous equation becomes:

$$I = I_c \sin\varphi + \frac{\hbar C}{2e}\frac{d^2\varphi}{dt^2} + \frac{\hbar}{2eR}\frac{d\varphi}{dt}. \tag{2.11}$$

The Josephson junction dynamics is analogous to the problem of a particle of mass

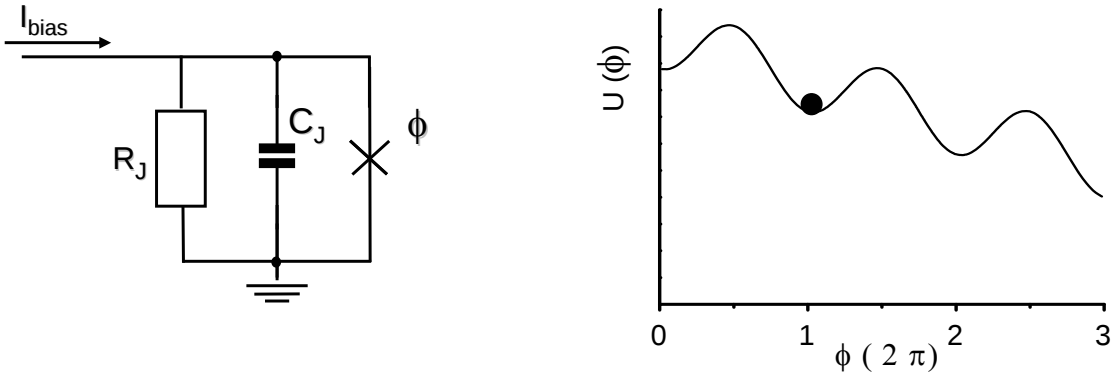

Figure 2.3: Left: Equivalent circuit of a Josephson junction used in the RCSJ model. Right: Washboard potential. The x–axis is the phase which corresponds to the position of the particle while the y–axis represents the total energy of the particle, with the kinetic energy indicated by the height of the particle above the washboard potential.

$(\hbar/2e)^2 C$ moving along the φ axis and subject to a potential $U(\varphi)$ of the form:

$$U(\varphi) = -E_J \cos\varphi - (\hbar I/2e)\varphi \tag{2.12}$$

in presence of a viscous drag force $(\hbar/2e)^2(1/R)d\varphi/dt$, as drawn in Fig. 2.3 (b). The tilting of the washboard potential is given by the bias current, it is zero when no current is applied and increases when the current flowing through the junction is increased. When the bias is small the phase can be trapped in a minimum of the potential, in this case we can approximate $\sin\varphi \sim \varphi$ and the junction dynamics is analogous to the motion of a damped oscillator. As for the oscillator, we can define a characteristic frequency, the so called *plasma frequency* ω_p, and the quality factor Q:

$$\omega_p = \sqrt{2eI_c/\hbar C} \tag{2.13}$$

$$Q = \omega_p RC. \tag{2.14}$$

The shape of the IV characteristics depends strongly on the strength of the damping. It is possible to distinguish two different behaviors depending on the value of the quality factor. When $Q \ll 1$, a condition typical for a small capacitance junction, the dissipation is strong and the junction is *overdamped*. In the limit $Q \gg 1$ the dissipation is low and the junction is called *underdamped*. Typical IV curves for the two different cases are

shown in Fig. 2.4, where the top graph refers to an overdamped junction and the bottom one to an underdamped.

As seen in Fig. 2.4 a typical signature of underdamped dynamics is a hysteretic IV characteristic. The IV curve depends on the sweep direction and this dependence reflects the difference between the transition from the zero voltage state to the resistive one and the reverse process, the transition from the normal to the superconducting state. We now introduce two useful concepts: the switching current I_{sw}, the current at which the junction switches from the superconducting to the normal state, and the retrapping current I_r, the current at which the junction jumps from the normal state to superconducting one. To understand why this hysteresis is appearing it is useful to consider the equivalent model of a particle in a washboard potential (see Fig 2.3). When the bias current is zero the potential is sinusoidal, but as soon as the current is increased the potential starts to tilt. In the limiting case of no damping and zero temperature the phase is trapped until the bias current reaches the value $I_{sw} = I_c$, then the phase if free to escape and the junction becomes normal conducting. The retrapping current is the current at which, when ramping down the bias, it is possible to trap the particle again. For the case of no damping this would happen only at zero bias current, while in case of finite but still strong damping $Q \ll 1$, it can be shown that the critical current and retrapping current are related by the following relation:

$$I_r = 4I_c/\pi Q \tag{2.15}$$

In the opposite case of strong damping $Q \gg 1$ all the kinetic energy is dissipated efficiently. As a result the particle slides along the washboard potential rather than escape from the trapped state. In this condition there is no jump in the IV and no hysteresis is observed.

If we would include finite temperature effects, we should expect that the energy at a given phase is changed in a stochastic way by an amount k_BT in a time scale on the order of RC. When fluctuations are strong the phase will escape from a minimum of the washboard potential *before* the intrinsic critical current I_c is reached. This phenomenon is usually referred as *premature switching* and will be analyzed in more detail in the next section. A finite temperature also affects the retrapping current, even though in a much less dramatic way. The current I_r increases slightly when the temperature is decreased. While this behavior can appear counterintuitive it can be explained by noting that fluctuations can also decrease the energy, hence favoring the retrapping process. If the damping is strong enough, the phase will not switch to a running state in presence of fluctuations. In this case the kinetic energy is dissipated by the drag

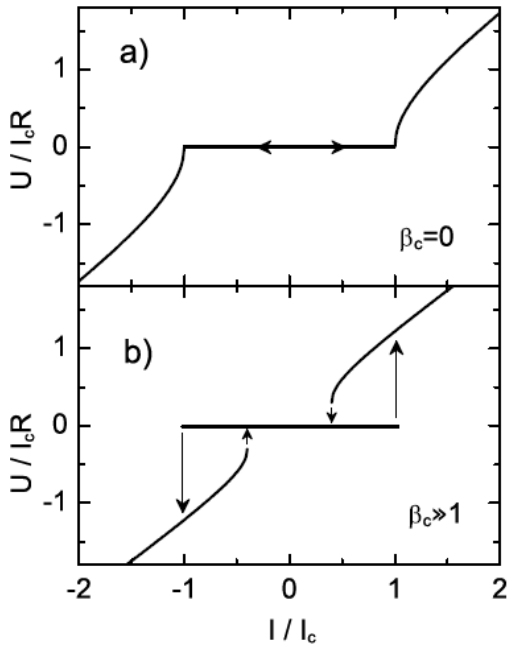

Figure 2.4: IV characteristic for an overdamped (upper graph) and underdamped (lower graph) junction at T =0. In the overdamped case no hysteresis is present and no switching is observed. In the underdamped case the IVs are hysteretic and the junction switches from the superconducting to the quasi particle branch at $I = I_{sw}$ and back at $I_r = I$.

force, and the phase will diffuse along the potential. This particular state is called phase diffusion and is characterized by a finite bias voltage even for a current $I < I_c$. The phase diffusion and the voltage across the junction are related by the second Josephson relation $d\phi/dt = 2eV/\hbar$.

2.5 Extended RCSJ model: effect of the environment and finite temperature

It was already mentioned that we expect that a finite temperature can induce a premature switching and reduce the value of I_{sw} below the critical current I_c. A proper model of the junction capable of taking into account these effects is essential to quantitatively determine the relation between switching current, which is the measured quantity, and

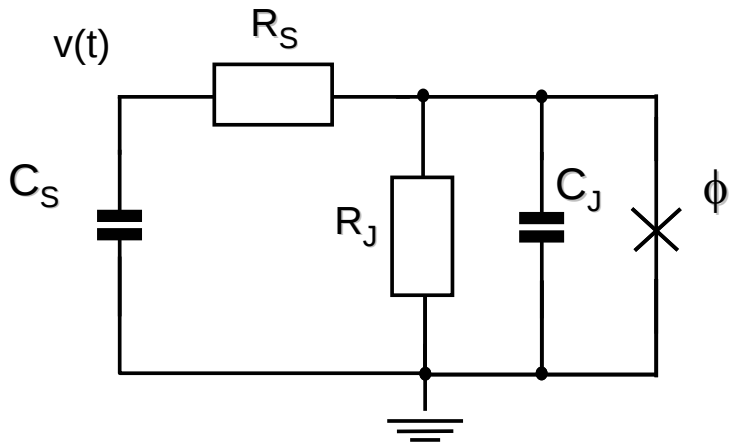

Figure 2.5: Equivalent circuit for the RCSJ extended model.

critical current which is usually the quantity of physical interest. The effects of thermal fluctuations are strong when the temperature is comparable to the coupling energy E_J, but they can be important even at lower temperatures, as it has been pointed out in several theoretical and experimental works. For junctions with low critical current, which are characterized by a small E_J, the thermal fluctuations have to be taken into account even at the lowest temperatures reached in experiments, which are typically on the order of few tens of millikelvin. We now describe an extension of the model presented in the previous section to include the electromagnetic environment and we analyze the effect of thermal fluctuations, which essentially requires solving the Langevin equation describing the system [31, 32]. The equivalent circuit for the extended $RCSJ$ model is sketched in Fig. 2.5.
We introduce two additional parameters:

(i) the McCumber parameter

$$\beta = \frac{2eR^2CI_c}{\hbar} \tag{2.16}$$

(ii) the normalized temperature (the fluctuation parameter)

$$\gamma = \frac{k_BT}{E_J} = \frac{2ekT}{\hbar I_c} \ . \tag{2.17}$$

The McCumber parameter is commonly used as a damping parameter and is related to the quality factor by the relation $Q = \beta^{1/2}$. The normalized temperature is the

ratio between temperature and coupling energy, or in other words, the ratio between thermal fluctuations and the height of the potential barrier E_J. After the inclusion of the electromagnetic environment, represented by the resistor R_S and the capacitor C_S, the system can be described by the following set of equations, where we use dimensionless variables $\tau = \omega_c t, j = I/I_c$, and $\omega_c = 2eRI_c/\hbar$:

$$\beta\frac{d^2\varphi}{d\tau^2} + \frac{d\varphi}{d\tau} + \alpha\left(\frac{d\varphi}{d\tau} - v\right) + sin\varphi = j + j_T + j_{Ts} \tag{2.18}$$

$$\beta\frac{dv}{d\tau} = \rho\left(\frac{d\varphi}{d\tau} - v - \frac{j_{Ts}}{\alpha}\right) \tag{2.19}$$

with j_T and j_{Ts} the current noise normalized to the critical current I_c, $\alpha = R/R_S$, $\rho = \alpha C/C_S$, and $v(t)$ is the voltage across the external capacitance C_S.
From a qualitative point of view the effect of the environment is to shunt the junction at high frequency. The value of the resistance R_S sets the damping at high frequency when the impedance of the capacitor is small. In this way it is possible to increase the damping at the plasma frequency, which is crucial to prevent the premature switching of the junction. Numerical simulations[2] show that there are three temperature ranges which exhibit a different behavior (Fig. 2.6):

- At low temperature ($k_BT \ll k_BT^*$ with $T^* = E_J/k_B$) the IV characteristics are hysteretic and the switching current measured in consecutive sweeps is randomly distributed around $< I_{sw} >$ that can be significantly lower than I_c. The broadening of the distribution is set by T and $T*$.

- At intermediate temperatures $T \sim T^*$ the curve shows a phase diffusion branch prior to the switch, and because of the diffusion of the phase along the washboard potential a small but finite voltage appears before the switching of the junction to resistive state. The hysteresis is also reduced when the temperature increases.

- At high temperature $T > T^*$ the hysteresis is completely suppressed and no switching is observed in the IV characteristics. A switching current I_{sw} can be defined as the maximum of the curve obtained by subtracting the linear term RI from the IV characteristics.

Fig. 2.7 shows simulation data for the temperature dependence of the switching current I_{sw} for a constant I_c. This is the main result of the theory: it predicts a strong suppression

[2]Code by Dr. D. Ryndyk

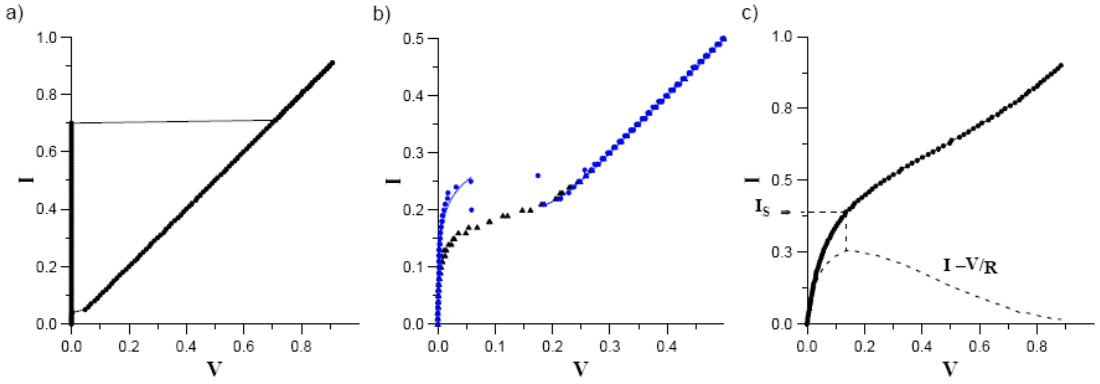

Figure 2.6: IV characteristics for three different temperature ranges. (a) Low temperature curve: the supercurrent branch has zero resistance and pronounced hysteresis is observed. The switching current is only 70% of the intrinsic critical current of the junction. (b) Intermediate temperature: the switching current is further reduced and the IV bends before the junction switches (phase diffusion). (c) High temperature: the IV is not hysteretical any more and no switching is observed. The I_{sw} is extracted from the maximum of the dashed line.

of the switching current due to thermal fluctuations for a temperature independent I_c. We should finally note that this model is exact only in the case of a sinusoidal current phase relation. Nevertheless, numerical simulations have shown that the model works very well also for junctions with intermediate and quite high transmission, while it starts to fail for transparency very close to 1. This is due to the fact that the two most relevant quantities are k_BT, the energy scale of the fluctuations, and E_J which is the barrier height. It is the ratio between these two quantities that determines the escaping probability and the switching of the junction, while the exact shape of the potential does not influence the result of the calculation much.

Switching histograms

It was already mentioned that the switching of the junction is a stochastic process if temperature effects are not negligible. The value of the switching current changes statistically if the measurement is repeated and it is distributed around an average value $< I_{sw} >$ with a certain statistics. The exact shape of the distribution can also be used to extract information about the junction dynamics and in particular about the switching

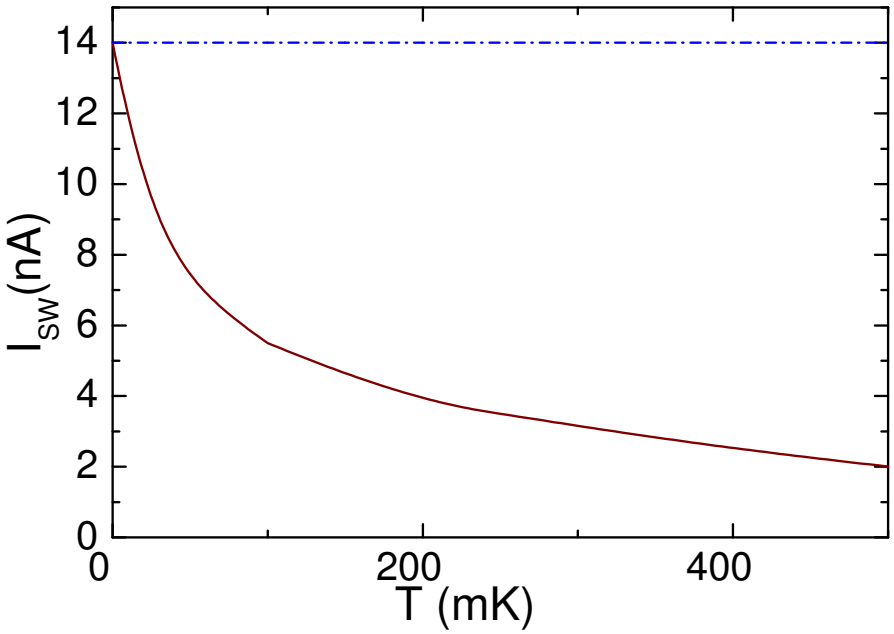

Figure 2.7: Temperature dependence of the switching current expressed in nA for a junction with $R = 10k\Omega$, $C = 0.2pF$, $R_S = 320\,\Omega$ and $C_S = 11pF$. The horizontal dashed line represents the temperature independent $I_c = 14\,\mathrm{nA}$ used for the numerical simulation. The switching current is strongly suppressed with respect to I_c.

mechanism.

Chapter 3

Experimental Details

In this chapter we present the sample design we developed and we briefly illustrate the sample preparation steps we used. In the second part we describe the experimental setup we employed for the different measurements presented in the following chapters.

3.1 Sample Layout

Previous experiments with carbon nanotube Josephson junctions showed that premature switching was responsible for suppressing the switching current well below the value of the critical current and that a very good filtering is essential to be able to observe supercurrent at all. We addressed this issues by designing an optimized electromagnetic environment that provides an effective damping at the plasma frequency and by using a very careful filtering scheme which includes several warm and cold filtering stages. A sketch of the sample layout is in Fig. 3.1.
In our design only two contacts are connected to the nanotubes, so that only the two point conductance can be measured. Nevertheless it is useful to have four terminals to separate current and voltage paths on the chip, since this measurement setup allow to get rid of the offset resistances that distributed along the lines.

3.2 Sample Preparation

A micrograph of a typical sample studied in this work is shown in Fig. 3.2. The samples were fabricated on a doped silicon substrate with a 400 nm thick oxide layer. Because of the high doping, the substrate can be used as a backgate down to very low temperature. We prepared an alignment mark grid by using standard electron beam lithography (EBL)

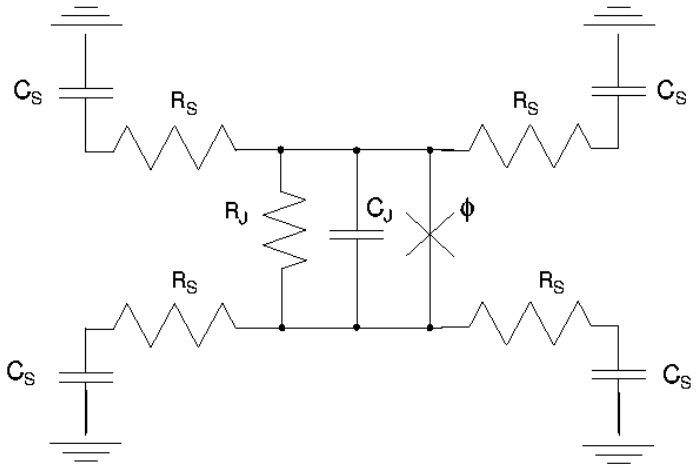

Figure 3.1: (a) Sketch of the sample layout.The on chip resistors R_S and capacitances $C + S$ are used to optimize the electromagnetic environment in which the junction is embedded.

and evaporating a Ti(5nm)/Au(60nm) bilayer. The thin titanium film is used as an adhesion layer. The high purity multiwall carbon nanotubes used in this work have been grown by arc-discharge by the group of L. Forro at the EPFL in Lausanne. We dispersed the raw nanotubes material in a solution of 1,2-dichlorobenzene (ODCB) by ultrasonication for thirty minutes, then we brought a droplet of the solution containing the nanotubes onto the substrate, we waited thirty minutes and then we flashed with propanol and blew dry with nitrogen to remove the solvent. As a result, the carbon nanotubes are randomly deposited and very strongly bound to the substrate by Van der Waals forces. We located the isolated nanotubes by using a scanning electron microscope (SEM) and recorded their positions with respect to the grid marks. While the SEM inspection may contaminate the nanotubes, it allows a fast search compared to the atomic force microscope. From the SEM pictures it is possible to identify kinks, inhomogeneities or catalytic particles that can lower the quality of the nanotube. We further processed only those tubes that presented a long part (at least 1 μm) free of such a type of defects.

For patterning the leads and the electrodes we used a two step electron beam lithography (EBL) process. First the leads were defined by standard EBL, then evaporated by

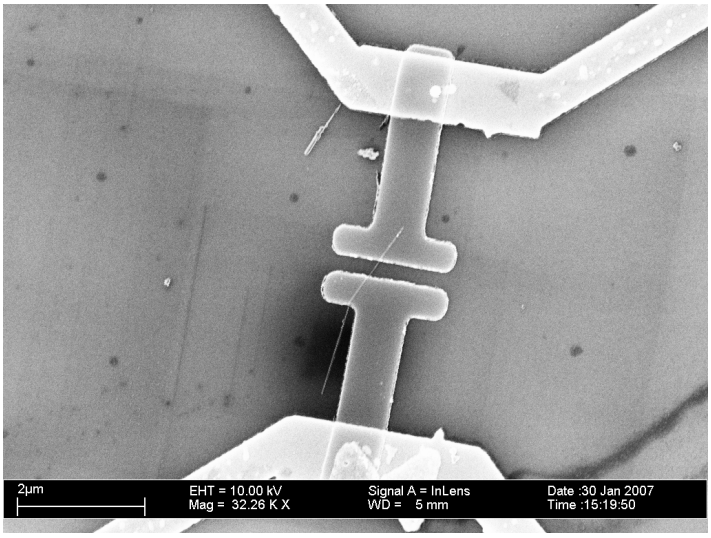

Figure 3.2: Micrograph of the sample: the nanotube lays between the niobium contacts. The part of the AuPd resistive leads are also on the figure.

using 5 nm of Ti as an adhesion layer followed by 65 nm of AuPd as actual lead and to provide the desired resistance for the electromagnetic environment. After lift-off we performed a second lithography step. The contacts were patterned and then prepared by evaporating first 3 nm of palladium followed by sputtering 45 nm of niobium in the same UHV run (appendix B). We note that the e-beam evaporation of niobium is difficult because the process temperature is too high for standard PMMA resist while thermally more stable materials like PES require an additional etching step that would destroy the tube. Sputtering results in a less clean lift off compared to e-beam evaporation, with typical flakes sticking at the edges of the patterned structure. It is obviously very important that such a flake does not shortcut the nanotube junction. This complication can be avoided by choosing the EBL resist layer thin enough (for our sample we use a thickness of the order of 150 nm). The on chip capacitance C_S was provided by the big bonding paths and the desired on chip resistance was obtained by pattering long and narrow constriction in the leads. The value of the resistance R_S and R_J where obtained directly from the measurements while the value of the capacitance where estimated by using a parallel plate capacitor model. A table resuming the obtained values are printed in Table.3.1. The samples were then glued on a chip carrier by using conducting silver glue and bonded with gold or aluminum wires.

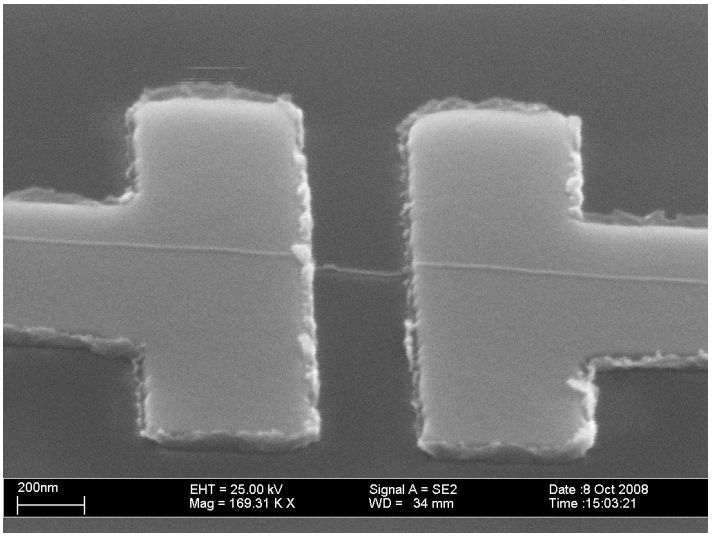

Figure 3.3: Close up of the PdNb-MWNT-PdNb junction. The flakes from the lift off are visible. The Pd/Nb layer is about 48 nm thick and lays on top of the nanotube. The view angle is 60 degrees.

The on chip resistors has been placed as close as possible to the sample. This is necessary because the fluctuations that are particularly effective in inducing premature switching are those of the order of the plasma frequency w_p $100GHz$, if the resistors are far away the junction is shunted by the distributed stray capacitances only, making the resistors useless.

C_J	0.2 pF
R_J	10 - 30 KΩ
R	160 Ohm
C	11.5 pF

Table 3.1: Typical values of the parameters describing the junction and the on chip resistive environment.

3.3 Measurement Setup

The measurements presented in this work has been performed using a Minidil dilution refrigerator from Air Liquide with a base temperature of about 25 mK and an Oxford HelioxVL helium three cryostat supplied from Oxford.
The Minidil cryostat is mounted in a massive copper box to shield electromagnetic and acoustic noise, each line entering the cryostat's box is filtered with π-filter. To ensure that the electron temperature is close to the bath temperature each line connected to the sample was filtered with an additional room temperature radio frequency π-filter stage and two low temperature copper powder filters mounted at the 1 K and 100 mK plates. The copper powder filters provide an excellent thermal anchoring and have a cutoff frequency of around 500 MHz, well below the blackbody radiation of the helium bath at 4.2K which is about 245 GHz. An extra two-stage low temperature RC filter was mounted at 4.2 K. A careful filtering in all the frequency range above 10 KHz is essential to prevent the premature switching of the nanotube Josephson junction and it is crucial to observe very low supercurrents (see Appendix).
The cryostat was equipped with a superconducting coil and an IPS Oxford power supply that can be used to apply magnetic field up to 8 Tesla. The magnetic field was applied perpendicular to the substrate, and therefore it was perpendicular to both, the nanotube and the contacts.
The helium three cryostat has a base temperature of 360 mK and is equipped with superconducting coil that can be used to generate magnetic fields up to 14 Tesla. We employed a room temperature π-filter and a low temperature stage of copper powder filters, but no low frequency RC filters were present. The lack of this filtering stage precludes the observation of a fully developed supercurrent, therefore this setup has been mainly used for Coulomb blockade measurements.
To minimize the ground loops all the instruments were powered through transformers, while for the most critical instruments, the current and voltage preamplifier, we used batteries.
We performed the measurements in a four terminal configuration, nevertheless the measurement is a two points measurement in the sense that the nanotube itself is connected to the leads only by two superconducting contacts. We used three main bias schemes according to the measurement preformed. The measurements were controlled by a computer connected to the instruments with a GPIB bus. The programs needed for the measurements and for the data analysis have been written as part of the work of this thesis.

Circuitry for measuring the IV characteristics

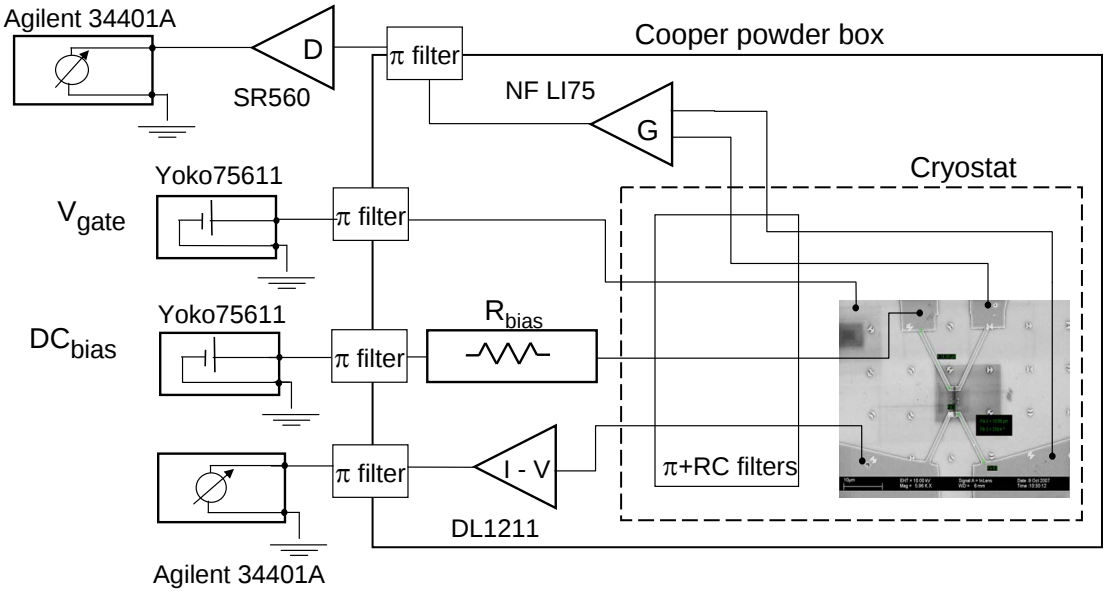

Figure 3.4: Setup used for measuring the IV characteristics. An alternative set up were the lock in is used as bias source and as a current detector as been used as well.

To measure IV characteristics we used a current bias scheme sketched in Fig. 3.3. The current was defined by applying a voltage source using a Yokogawa7561 and resistor of typically 100 M Ω or 1 GΩ, much bigger than the sample resistance in the normal state. The current flowing through the sample has been converted to a voltage by a DL 1211 current amplifier and measured with an Agilent 34401A multimeter. The dc-voltage drop across the sample was first amplified with a NF-Electronics LI-75 Voltage Amplifier and measured with a second Agilent 34401A multimeter3.3. A similar setup with lock-in in series with the Yokogawa has been used for measuring the differential conductance directly.

Switching statistics

The study of the statistics of the switching requires to repeat the measure of the switching current for several thousand times. The set up we used consist of a pulse generator DS345 from Stanford Research System and a bias resistor which is used to send current to the sample, a voltage amplification stage (NF-Electronics LI-75 and SR560 with a low pass

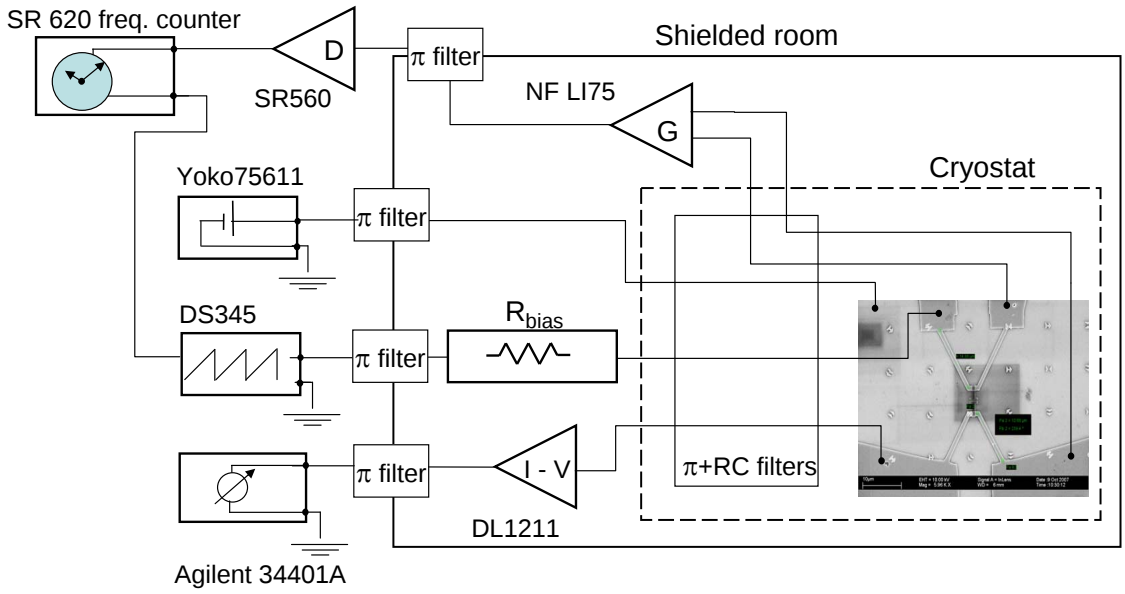

Figure 3.5: To measure the switching statistics we used a pulse generator to generate a sawtooth wave that bias the junction. When the pulse is started the frequency counter starts to count. The counter is stopped once the junction switches to the resistive state.

filter of around 10 KHz), and a Stanford SR620 frequency counter. The two inputs of the frequency counter are connected to the TTL trigger of the pulse generator and to the output of the SR560. The measurement principle is quite simple: we used a pulse generator to produce a sawtooth wave and a big input resistor to current the bias the junction. When the pulse is started, a signal is sent to the frequency counter that starts a timer. The second input of the frequency counter is used to stop the counter and is connected to the output of the amplifier which monitors the voltage across the nanotube. This voltage is zero (or close to zero in the case of phase diffusion) when the junction is superconducting and jumps to a finite value after the switch to the quasi particle branch. The frequency counter can be programmed to stop counting when the input signal exceeds a given threshold (which has to be chosen between zero and the voltage in the normal state). The time interval measured can then be converted in current by knowing the sweeping rate of the pulse generator. Typically we used a sweep time of the order of 1-100 millisecond.

Coulomb blockade

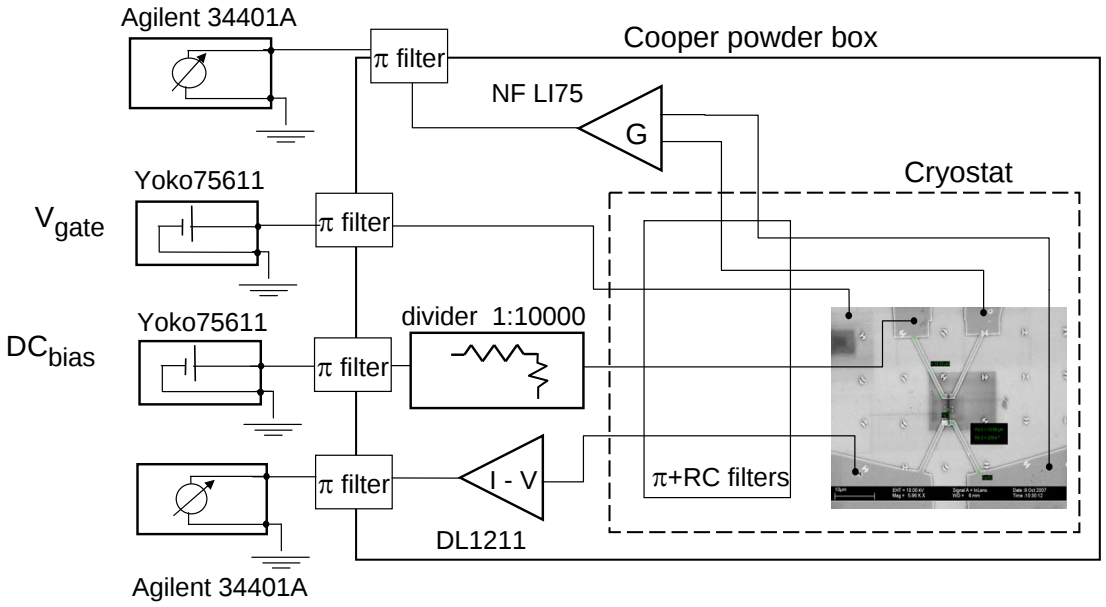

Figure 3.6: Setup used for the measurements in the Coulomb blockade: a voltage divider is used to voltage bias the nanotube. The four terminal configuration allows to measure voltage across the nanotube and the current flowing through the sample.

To measure the stability diagrams we adopted DC and AC setup depending on the cryostat used. The low temperature RC filtering limits the bandwidth to less then 1 Hz (depending on the resistance of the sample) so that lock-in measurements become too slow. In the DC setup a constant voltage is applied to the sample with a Yokogawa7561 and a voltage divider 1:10-4. The current flowing through the junction was then converted to a voltage with a current amplifier DL 1211, amplified by the SR560 amplifier and measured with an an Agilent 34401A multimeter. The voltage drop across the sample was measured using a Agilent multimeter connected to the LI-75 preamplifier. The 2D differential conductance plots are obtained by numerically interpolating and differentiating the measured IV characteristics. For AC measurements a lock-in was added in series to the Yokogawa and used to read the output of the current amplifier.

Chapter 4

Supercurrent

This chapter focuses on the study of the supercurrent in our nanotube Josephson junctions. We present the measured IV characteristics and we compare them with those obtained with the extended RCSJ model presented in Chap. 2. We discuss the temperature dependence of the switching current I_{sw} and we use the extended RCSJ model to extract the intrinsic critical current for a supercurrent resonance. We performed measurements of the magnetic field dependence of I_{sw} and we compare the effect of magnetic field and temperature. The statistical distribution of the switching current is also analyzed. Finally we discuss the origin of the resonant behavior of the supercurrent.

4.1 Preliminary measurements

We tested the quality of the niobium used in our carbon nanotube Josephson junctions by measuring a Pd(3nm)/Nb(45nm) reference stripe. We used a four terminal design similar to the one implemented in our CNT-JJ and we chose the geometrical size of the reference stripe close to that used for contacting the nanotubes. The measured differential resistance drops to zero at about 6.9 K, not too far from the bulk value of 9.26 K. This discrepancy is caused by the small dimensions of the stripe and by the presence of the thin palladium layer underneath the superconductor. The proximity induced gap of the bilayer is indeed expected to be reduced with respect to that of bulk niobium, moreover the density of states is modified with respect to that of a perfect BCS superconductor [33]. The critical field B_C depends only slightly on temperature below 1 K, where $B_C \approx 3$ T.

We tested seven samples at room temperature and we found resistances between 5 and 10 kΩ. This indicates a good electrical contact as can be expected for palladium which

is known to make excellent contact to carbon nanotubes [34, 35]. This contact scheme is reliable and allows us to fabricate relatively transparent interfaces in a reproducible way, which is essential for studying proximity induced superconductivity.
A first CNT-JJ was measured in a dilution refrigerator where only room temperature RC and π-filters were mounted. Despite the on chip resistive electromagnetic environment, we were not able to observe a dissipationless supercurrent, but only a precursor of the supercurrent was found for several gate voltage regions. The precursor was seen as a narrow peak in the differential conductance at zero bias. This measurement that will be discussed in more detail in Sec. 4.5 confirms that low temperature filters are crucial to observe supercurrent in such a small Josephson junction.

4.2 Sample Characterization

In the following we will mainly focus on one of the two samples where supercurrent was observed. The sample was cooled down several times and while the details of the measurements are slightly different after each thermal cycle, the overall behavior is unchanged. This is a well know phenomenon and it is due to a change in the nanotube doping configuration.
To characterize the sample we recorded the linear conductance as a function of the applied gate voltage V_G, from room temperature down to 360 mK. These measurements were performed in a ^{3}He cryostat $without$ a low temperature RC filter stage. The results are shown in Fig. 4.1. At room temperature the conductance is very smooth and shows a shallow minimum around $V_G \approx -3\,\mathrm{V}$. When the temperature is reduced the minimum becomes more pronounced and, for temperatures below 50 K a "gap" develops for $-5\,\mathrm{V} \leq V_G \leq -2.5\,\mathrm{V}$. Moreover, at low temperature the conductance is reduced and the gate voltage modulation increases. At 360 mK the transport at positive gate voltages is dominated by charging effects and Coulomb oscillations are observed. At negative gate voltage the conductance is still strongly modulated by the gate but we do not observe Coulomb blockade, indicating a higher transparency of the contacts. When the temperature is low enough multishell conductance and thermal excitations are strongly reduced and a gap-like suppression of the conductance is observed in the measurements. Inside the gap we also observed small Coulomb peaks which we interpret as charging of an inner shell. This will be briefly discussed in the next chapter.
Experiments on small gap semiconducting SWNTs with palladium contacts have shown that a higher transparency is expected at negative gate voltages [36, 37]. This behavior

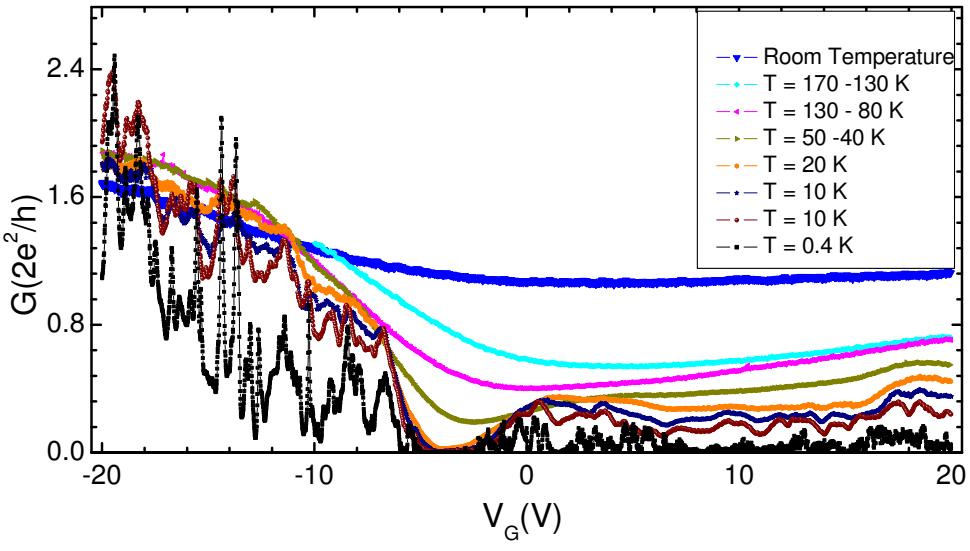

Figure 4.1: Linear conductance as a function of gate voltage for several temperatures, from room temperature down to 360 mK. Below 20 K the conductance around $V_G \approx -3$ V is strongly reduced. The conductance is higher at negative gate voltages, while at positive gate voltage and low temperature the transport is in the Coulomb blockade regime.

has been successfully explained as a consequence of a small Schottky barrier for holes, due to the fact that the work function of palladium is close to the valence band edge of a semiconducting carbon nanotube. When the gate voltage is used to shift down the energy bands of the nanotube so that transport is due to electrons rather than holes, a bigger Schottky barrier is formed and the transparency of the contacts is reduced.This explanation is consistent with the observed gate dependence of the linear conductance and with the assumption that the high resistive region around zero corresponds to the gap of the outermost semiconducting shell of our multiwall nanotube. The different transparencies for negative and positive gate voltages leads to opposite behavior at low temperature: in the first case we observe supercurrent while in the second the transport is blocked by Coulomb interaction.

The measurements presented in the following were performed in our Minidil dilution refrigerator equipped with the complete filtering scheme required to investigate super-

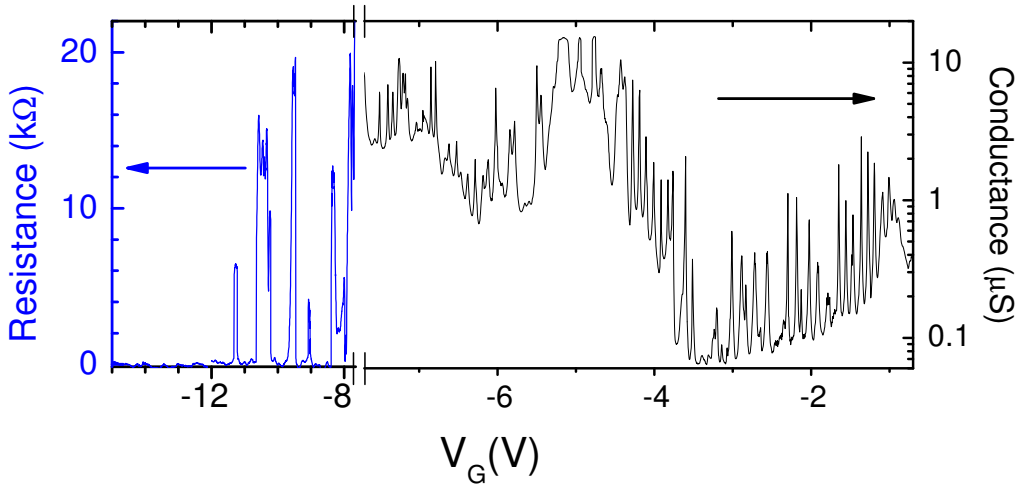

Figure 4.2: Transition from a high transparency regime at negative gate voltage V_G (left) with partially vanishing resistance (blue) to a Coulomb blockade regime with partially vanishing conductance (black) at more positive V_G (right). The measurements were taken at 25 mK in our fully filtered dilution refrigerator.

current. The linear conductance measured at 25 mK is plotted in Fig. 4.2. For gate voltages $V_G > -8\,\mathrm{V}$ the conductance is rather low ($G < 15\,\mu\mathrm{S}$) with a transition to nearly equidistant Coulomb peaks above -4 V ($G < 3\mu\mathrm{S}$). For $V_G < -8\,\mathrm{V}$ the resistance remains below 20 kΩ and drops to zero in certain regions. For $V_G < -12$ V the sample is superconducting. At a gate voltage around $Vg \approx -3\,\mathrm{V}$ the Coulomb blockade is particularly effective. A second sample measured at low temperature showed also a similar behavior, with supercurrent at negative or small positive gate voltage and Coulomb blockade for positive gate voltages, pointing to a higher transparency at negative gate voltages.

4.3 Superconducting resonance

We now focus on the negative gate voltage region where proximity induced supercurrent was observed. We measured the switching current I_{sw} as a function of the applied gate voltage by sweeping the bias current upward and recording the current at which the

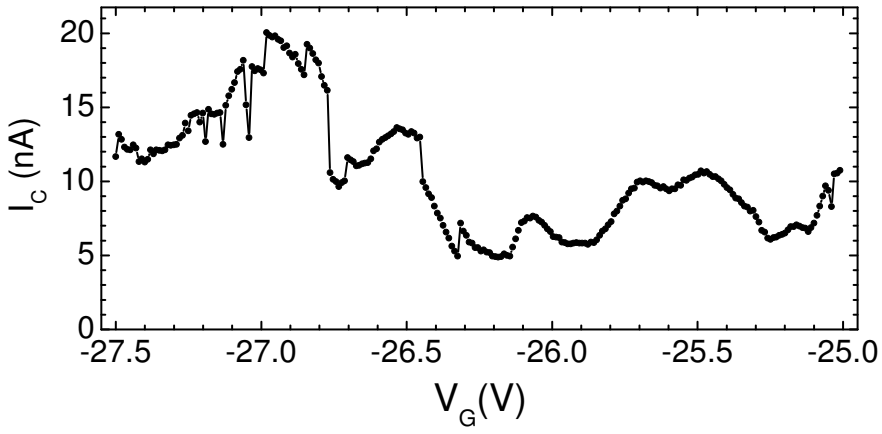

Figure 4.3: Switching current versus gate voltage measured at 25 mK. The overall critical current is high and shows a resonant behavior with several resonances merging together. At high negative gate voltage we observe strong switching due to movements of charge traps.

junction jumps from the supercurrent to the resistive branch. The measurements were performed in the current bias setup described in Chap. 3.

We found a pronounced resonant behavior. When the gate voltage is tuned more negative the average value of the switching current tends to increase and several resonances merge, as shown in Fig. 4.3. The maximum value of I_{sw} observed was 31 nA. At high negative gate voltages movements of trapped charges induce abrupt changes in the value of the switching current and the resistance. These values of the switching current are high compared to previous reports on carbon nanotubes [38, 39, 40]. With the exception of one early work on suspended and non gated nanotubes where switching currents up to several hundreds nanoamperes have been measured [41], only switching currents up to about 6 nA have been reported in SWNT. We are aware of only one work on gated MWNTs with superconducting contacts where a maximum switching current of 1.3 nA has been observed [40]. Critical currents on the order of a few nanoamperes have been extracted from the non linear IV in several works on single wall nanotubes contacted with superconducting contacts even though a fully developped supercurrent was not measured [42, 37, 43]. These works were done using aluminum as a superconductor.

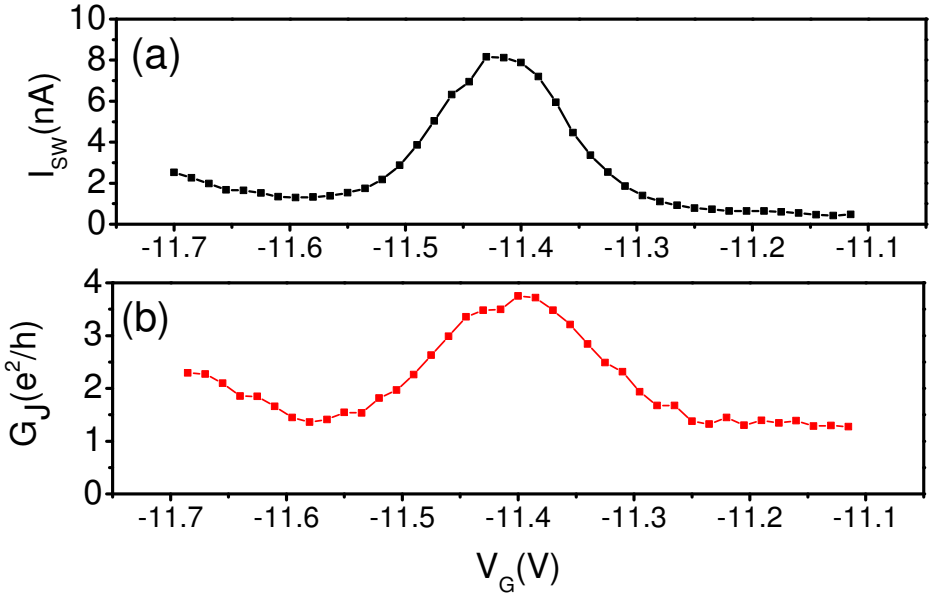

Figure 4.4: (a) Switching current resonance around $V_G \approx -11.4\,\mathrm{V}$, measured at 25 mK. The maximum switching current is around 8 nA. (b) Conductance G_J extracted from measurements in the resistive branch with the contacts in the superconducting state.

For a short Josephson junction with $\Delta < E_{Thouless}$ the higher gap of the niobium is expected to increase the critical current of the junction with respect to the case of aluminum contacts by a factor of $\Delta_{niobium}/\Delta_{aluminum}$.

To get a deeper insight to the proximity effect in multiwall carbon nanotubes we studied an isolated resonance centered at gate range $V_G \approx -11.4\,\mathrm{V}$ in more detail. The switching current versus gate voltage for such a resonance measured at 25 mK is plotted in Fig. 4.4 (a). The resonance extends over a gate voltage range of about 0.3 V which is bigger than average peak spacing $\delta V_G \approx 70\,\mathrm{meV}$, measured in the Coulomb blockade region. Therefore we can exclude that the resonance is due to a single broadened Coulomb peak. When using niobium contacts the value of the normal state conductance is not easily accessible. In order to drive the contacts into the normal state we need to apply a magnetic field greater than 3 Tesla. Such a strong field influence the transport within the nanotube in a non trivial way. We performed such a measurement at $B = 6\,\mathrm{T}$

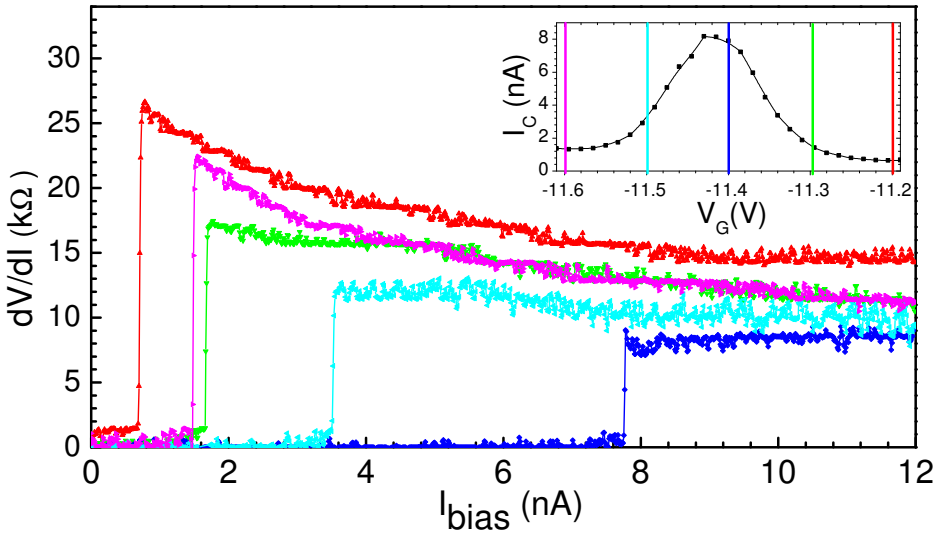

Figure 4.5: Differential conductance for several gate voltages across the superconducting resonance at $V_G \approx -11.4\,\mathrm{V}$. When tuned off the resonance, the switching current decreases while phase diffusion becomes more pronounced reflecting the decrease of the coupling energy E_J. The inset is a plot of I_{sw} for such a resonance, where color bars indicate at which gate voltage the dV/dI traces plotted in the main figure were taken.

(not shown) from which we could confirm that the sample does not behave like a single electron transistor in the Coulomb blockade regime.

Although we could not measure the normal state conductance directly, experiments on SWNTs with titanium contacts [42] have shown that the conductance G_J in the resistive branch (measured at high current bias $I > I_c$) follows that of the normal state. Fig. 4.4 (b) shows the value of the conductance G_J for our sample that clearly shows a resonant behavior that is also observed in the gate dependence of the switching current. The gate dependence of the switching current I_{sw} is much more pronounced than that of the conductance: I_{sw} changes by a factor of 15 across the resonance while G_J only by a factor of 3. This behavior is in qualitative agreement with what is expected from a quantum dot coupled to superconducting leads where both R_N and I_c exhibit a resonant behavior [44]. We argue that the nanotube behaves like an open quantum dot (similar to what was reported in ref. [38]) where due to the relatively high coupling to the leads

the charge fluctuations are strong. The size of the resonance is compatible with the addition of four to six electrons. Multiwall nanotubes are usually a less clean system compared to SWNTs, and therefore the sample breaks into several dots in series. For this sample Coulomb blockade measurements (presented in the next chapter) shows that the nanotube behaves like a single quantum dot.

More informations can be extracted by taking a closer look at the shape of the IV characteristics and at their temperature dependence. We recorded dV/dI versus I_{bias} as a function of temperature and gate voltage. For the gate voltage corresponding to the resonance at $V_G \approx -11.4\,\mathrm{V}$ we swept the bias current from 0 up to 12 nA. The dV/dI curves for 6 gate voltages across such a resonance measured at $T = 27.7\,\mathrm{mK}$ are shown in Fig. 4.5. At low current the junction is in the superconducting state and the resistance fluctuates around zero. When the bias is swept, and prior to switching to the resistive state, the resistance becomes finite indicating phase diffusion. When the current reaches a certain value I_{sw} the junction switches to the resistive state and a resistance R_J on the order of 10-20 kΩ is measured. When the gate voltage is tuned off of the center of the resonance we find that the switching current decreases while the resistance in the phase diffusion increases. The decrease of the switching current is due to a decrease of the coupling energy E_J and of the intrinsic critical current I_c, which are linked by the relation $E_J = I_c \cdot \hbar/2e$. The decrease of the coupling energy E_J, which is essentially the potential barrier seen by the phase in the washboard potential, results in a stronger diffusion of the phase which corresponds to an increase of resistance. The measured curves are hysteretic, with a stronger hysteresis for higher switching currents (not shown for this resonance). The observed behavior is in agreement with predictions from the extended RCSJ model discussed in Chap. 2 at intermediate temperatures.

We found a similar behavior when the gate voltage is kept fixed and the temperature is increased. Also in this case the switching current is suppressed and the phase diffusion becomes more pronounced. We note that this is expected also for a constant critical current $I_c(T) = I_c(T = 0) = I_{c0}$. In this case the reduction of I_{sw} is due to thermal fluctuations rather than to a decrease of the coupling energy (and therefore of I_c). We used the extended RCSJ model to interpret the results of our measurements.

Fig. 4.6 (a) is a plot of the measured dV/dI curves for $V_G = -11.4\,\mathrm{V}$ and the numerical simulations obtained using the RCSJ extended model for a temperature independent critical current $I_c = 14\,\mathrm{nA}$ (b). The value of the electrical elements necessary to model the junction and the electromagnetic environment are either measured or estimated with a simple geometrical model as discussed in Chap.3. The agreement between the switching

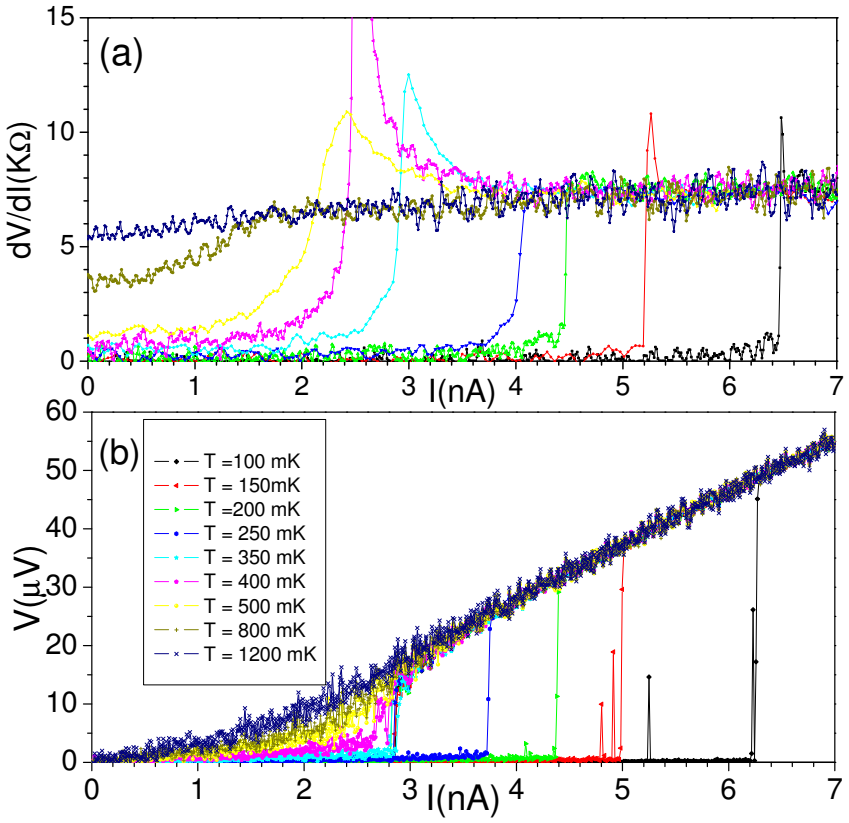

Figure 4.6: (a) Measured differential conductance as a function of bias current for several temperatures. The current is swept from zero to 7 nA. The increase of temperature reduces the switching current and results in a higher phase diffusion. (b) IV characteristics obtained with the extended RCSJ model and a critical current $I_c = 14\,\mathrm{nA}$. Equal colors in the two graphs correspond to the equal temperatures.

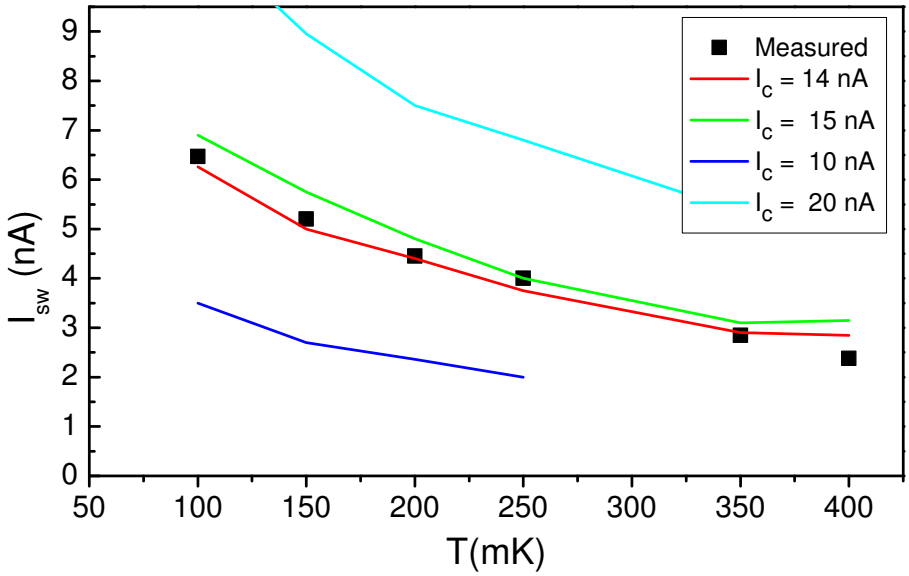

Figure 4.7: The switching current as a function of temperature calculated using the extended RCSJ model for several values of I_c (line) is compared to experimental data points (dots).

currents extracted from the measured data and from the simulations is good even though not perfect. The theoretical data correctly reproduces the behavior of our sample. At low temperatures I_{sw} is higher and only a small phase diffusion branch is observed. When the temperature increases the switching current is suppressed and the phase diffusion becomes stronger, at high temperature the junction does not switch anymore and also the hysteresis vanishes. We tested the accuracy of the estimated critical current by repeating the IV simulations for several values of the critical current. The values of the switching currents as function of temperature for $I_c = 10, 14, 15, 20$ nA are plotted in Fig. 4.7.

The main reduction of the switching current for temperatures up to about 400 mK is due to thermal fluctuations while for higher temperatures the measured switching current seems to be lower than that predicted by the RCSJ model. At higher temperature the IVs do not switch anymore but are highly non linear. Fitting these measurements could allow to extract the critical current also for higher temperature and to complete the information about the temperature dependence of the critical current. We indeed expect that when the temperature is high enough also the intrinsic critical current becomes temperature dependent.

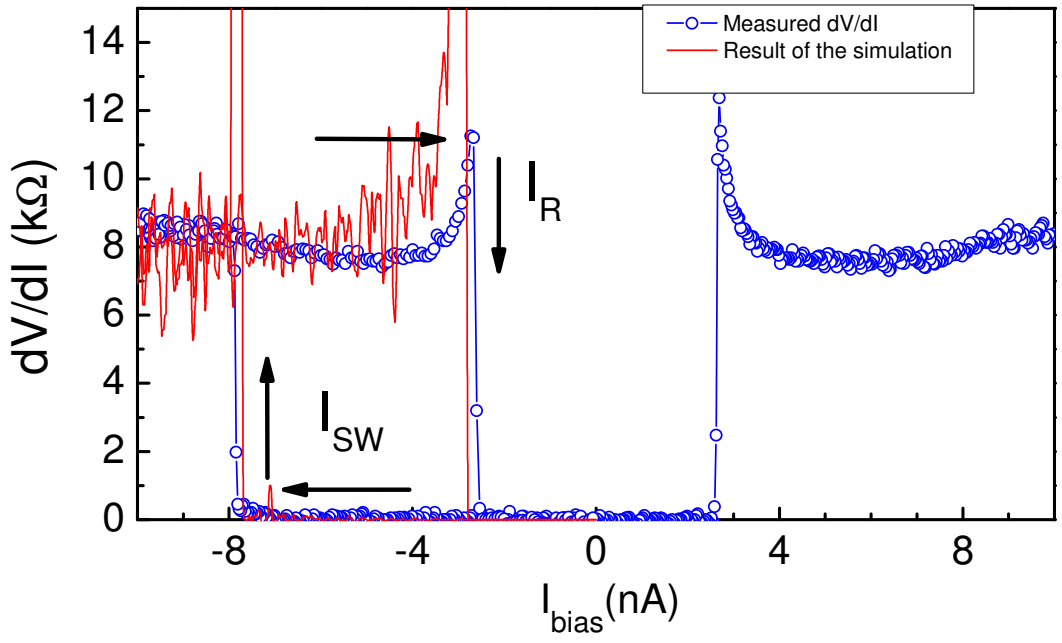

Figure 4.8: Differential conductance, measured data (open dots) and simulated data(red line) at $T = 50\,\mathrm{mK}$ and $V_G = -11.4\,\mathrm{V}$. The retrapping current is well reproduced without any free parameter, since $I_c = 14\,\mathrm{nA}$ is obtained from the T dependence of the switching current.

To verify the applicability of our model it is useful to look at the retrapping current I_r. The retrapping current is determined by the critical current and the damping of the junction and it is expected to be only slightly temperature dependent if I_c is temperature independent. Fig. 4.8 is a plot of the measured dI/dV characteristic for $V_G = -11.4\,\mathrm{V}$ and the dI/dV obtained from the extended RCSJ model with $I_c = 14\,\mathrm{nA}$. The theoretical data correctly reproduce not only the switching current but also the retrapping current I_r. It worth noting that the theoretical curve is obtained without any free parameter since the value $I_c = 14\,\mathrm{nA}$ was extracted from the temperature dependence of the switching current. The temperature dependence of the retrapping current is expected to be very small in the extended RCSJ model and this is also observed in our measurement (fig. 4.9). The retrapping current is almost constant for temperatures up to 500 mK, in agreement with a suppression of the switching current mainly due to thermal fluctuations rather than to a reduction of the coupling energy.

The supercurrent can be estimated using the model proposed in ref. [44]. The value of

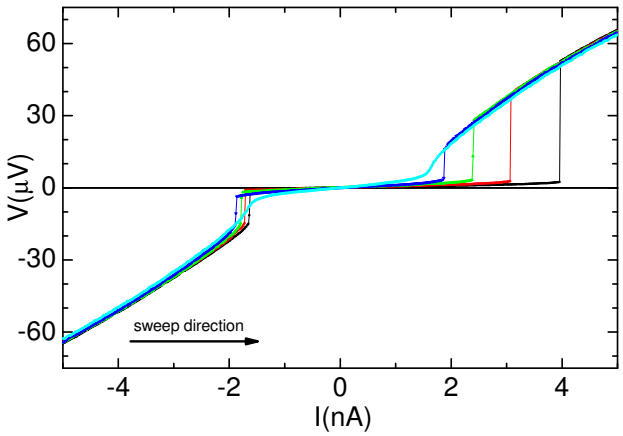

Figure 4.9: The retrapping current is almost temperature independent as expected for a constant coupling energy. This supports the applicability of the extended RCSJ model. The IVs have been measured at V_G = - 22.3 V. Similar behavior is observed for all the gate voltages we studied.

the critical current through a quantum dot is determined by the gap of the superconducting contacts and by the transmission of the Breit-Wigner resonance T_{BW} according to equation:

$$I_c = \frac{2e\Delta}{\hbar}(1 - (1 - T_{BW})^{1/2}) \tag{4.1}$$

The determination of the trasmission T_{BW} for our junction is difficult since the normal state conductance cannot be measured directly, in contrast to the case of aluminum contacts. The value of R_N we used to extract T_{BW} has been obtaind from the measurements at very high bias current. This value seems consistent with the average value of the conductance in high magnetic field. It can be used to get a rough estimate of I_c. With $\Delta = 0.8\,$meV for the Pd/Nb bilayer [33] and $T_{BW} = 0.4$ from the estimated value of R_N we get a critical current $I_c \approx 80$ nA. This value is higher than the 14 nA obtained from the fit of the temperature dependence of the switching current. Theory predict that finite lenght effects and electron interaction in a double barrier junction can decrease the critical current of the junction [45]. Disorder can also limit the value of the critical current if the Thouless energy E_{Th} is smaller than the superconducting gap Δ. When the coupling between the dot and the contacts is very high the junction is best described using the theory for S-N-S junctions [29]. In this case all the properties of the

junction are set by the length of the junction and the diffusion constant via the Thouless energy $E_{Th} = hD/L^2$. This model has been used in ref. [40] to explain the value of the observed critical current. Although we cannot exclude that disorder plays a role in our nanotube junction, the barriers at the contacts seem to play a major role and to account for the sharp resonant behavior of the critical current that we observed over a wide gate range. A systematic study of the critical current for different spacing L between the superconducting contacts would be desirable to clarify this point. This applies also to SWNT, since all the experiments reported so far on nanotube Josephson junction seem to extract a critical current that is lower than what is predicted by theory.

We performed the analysis of the temperature dependence of the switching current for several gate voltages around the resonance and for each gate voltage we extracted the corresponding critical current. The results are summarized in Fig. 4.10.

To conclude this section we comment on the numerical simulation: The model we used to analyze the data is based on the value of the electrical components that form the sample plus the on chip environment. Some of these parameters, in particular the capacitances, are not directly measured but estimated with a simple geometrical model and are therefore one possible source of error. Therefore we tested our model for different values of the capacitances and we found that the result does not depend strongly on these values. A factor of 2 in the capacitances results in a change of the critical current on the order of 10%. We should remark that our sample does not allow to directly measure the current phase relation which in our model is assumed sinusoidal. Numerical simulations have shown that the exact shape of the washboard potential does not influence strongly the average value of the switching current, while it can influence the phase diffusion and the switching statistics.

4.4 Magnetic field dependence

The effect of a magnetic field in conventional Josephson junctions has been the subject of several theoretical and experimental works. More recently, motivated by experiments on SWNTs with Al contacts, a model for magnetic field pair-breaking and the effect on both the critical current and the current phase relation for a quantum dot well coupled to superconducting leads has been proposed [46]. Previous experiments were done with superconductors that have a very low critical field, so that an experiment aimed to verify such a theory is problematic to conduct. In our case the niobium contacts exhibit a critical field up to several Tesla and therefore are more suitable for this goal. We found

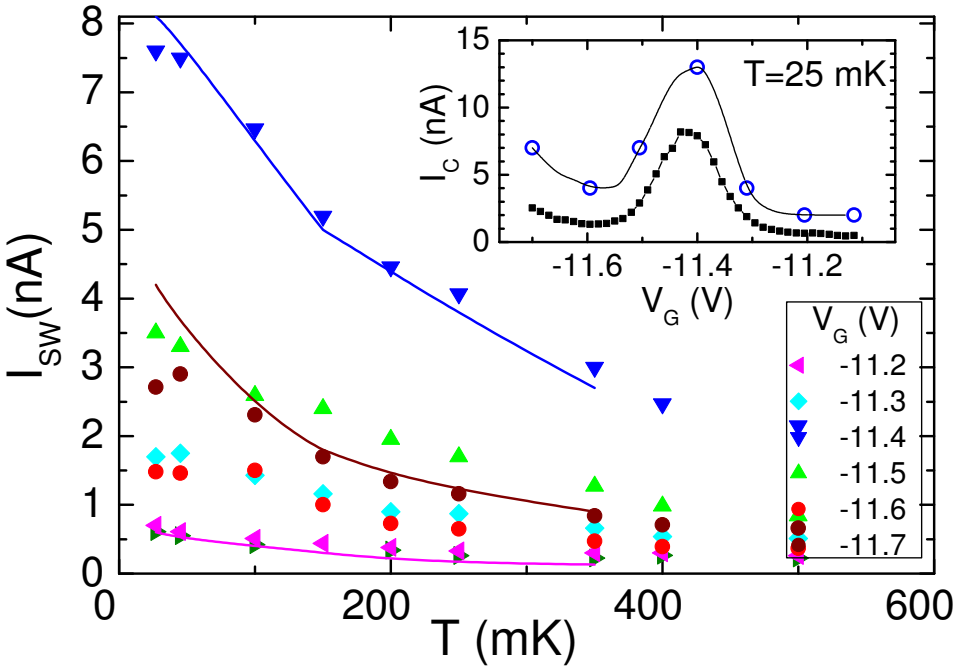

Figure 4.10: Temperature dependence of the switching current for different gate voltages. The solid line is a fit to the data obtained from the thermal fluctuation theory. The inset shows the measured switching current (solid dots) together with the values of the intrinsic critical current I_C extracted from the fits.

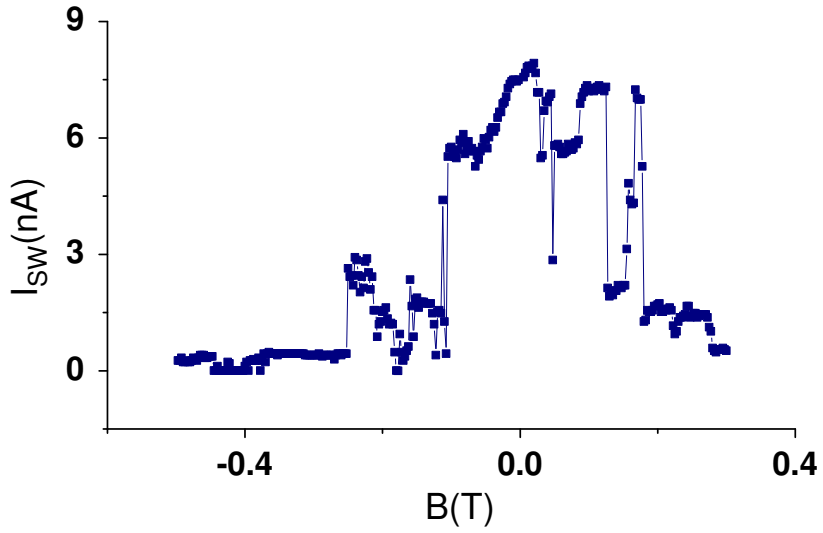

Figure 4.11: Switching current vs magnetic field measured at $V_G = -11.4\,\mathrm{V}$. Because of charge traps the critical current is subject to sudden changes. It is nevertheless possible to observe that switching currents up to several nanoamperes can be measured for magnetic fields up to about 250 mT.

that the critical current of the junction is quite robust with respect to magnetic field. Unfortunately measurements for $V_G \leq -11.4\,\mathrm{V}$ where the critical current is rather high are influenced by movements of charge traps that become very strong as soon as the magnetic field is increased. This can be clearly seen in Fig. 4.11. We therefore studied a gate area closer to zero gate voltage even though the critical current is lower. Fig. 4.12 shows the effect of the magnetic field B on the switching and the retrapping current. When B is increased both I_{sw} and I_r are clearly suppressed. The effect of magnetic field is therefore different from that of temperature (at least up to about 400-500 mK) where the switching current is suppressed but the retrapping current is almost constant. This is consistent with a suppression of the coupling energy E_J by the applied magnetic field B that is reflected in both I_c and I_r. On the other hand we have seen that an increased temperature does not affect the coupling energy E_J so that I_r is almost constant, while the switching current is still suppressed by thermal fluctuations.

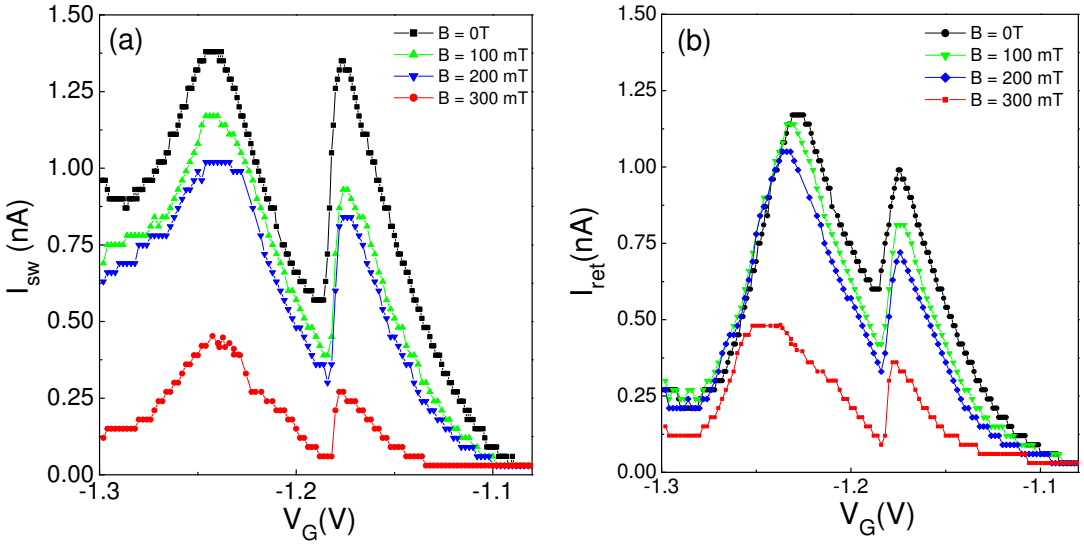

Figure 4.12: Switching current (a) and retrapping current (b) as a function of gate voltage measured at B = 0, 100, 200, 300 mT. Both the retrapping and the critical current decreases when the magnetic field is increased.

4.5 Multiple Andreev reflections

When the sample is voltage biased Andreev bound states do not exist anymore and a dissipative current flows through the junction. The microscopic mechanism that allows charge transfer between the two superconducting reservoirs are the so called *Multiple Andreev Reflections* (MAR). MARs are responsible for the ac Josephson effect described for a tunnel junction by the equation $d\phi/dt = 2eV/\hbar$. From a phenomelogical point of view, the MAR processes manifest themselves in the so-called "subharmonic gap structure" in the current-voltage characteristics of the junction: current singularities at voltages $V = \Delta/en$, with n = 1,2, . . , where Δ is the superconducting energy gap of the junction electrodes. Fig. 4.13 shows the result of our measurements of the diffential conductance performed in a voltage bias setup in our ^{3}He-cryostat. We do not observe any clear subgap structure, and similarly we do not see MAR in the Coulomb blockade measurements presented in the next chapter. This could be due to several factors, like the transparency of the contacts or a too short phase coherence length. MAR have been

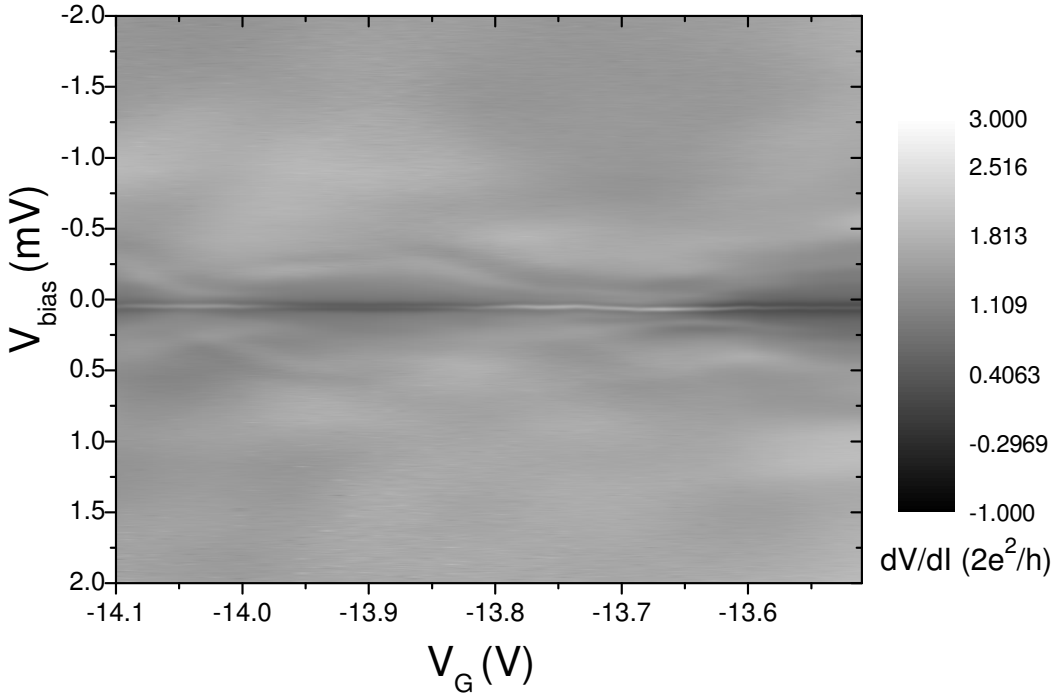

Figure 4.13: Measurements in a voltage bias setup: precursor of the supercurrent is observed at zero bias for some gate voltages. We do not observe clear subgap structure due to MARs.

observed in both SWNTs and MWNTs but a satisfactory match between theory and experiments has not been obtained.

4.6 Switching Histograms

A deeper insight into the switching mechanism can be obtained by studying the statistics of the switching current. The escape from a trapped state into a runaway state is triggered by the fluctuations. It is therefore a stochastic process so that information can be extracted not only from the average value of the switching current I_{sw} but also from the second momentum of the distribution. Two typical histograms measured for our sample are shown in Fig. 4.14.

We extracted an average value of the switching current and the standard deviation from each set of data, typically composed of 5000 to 10000 measurements of the switching

current. We fixed the gate voltage and repeated the measurement for several temperatures. Although the measurements are still preliminary and a more systematic analysis is required, the data shows that both the average switching current and the broadening of the distribution decreases when the temperature is increased. The temperature dependence of the broadening is qualitatively in agreement with that observed in a superconducting atomic contact with a similar damping, where the increase of temperature is found to reduce the randomness of the switching. We also note that the distribution is narrow, as it is expected for a junction with intermediate to strong damping.

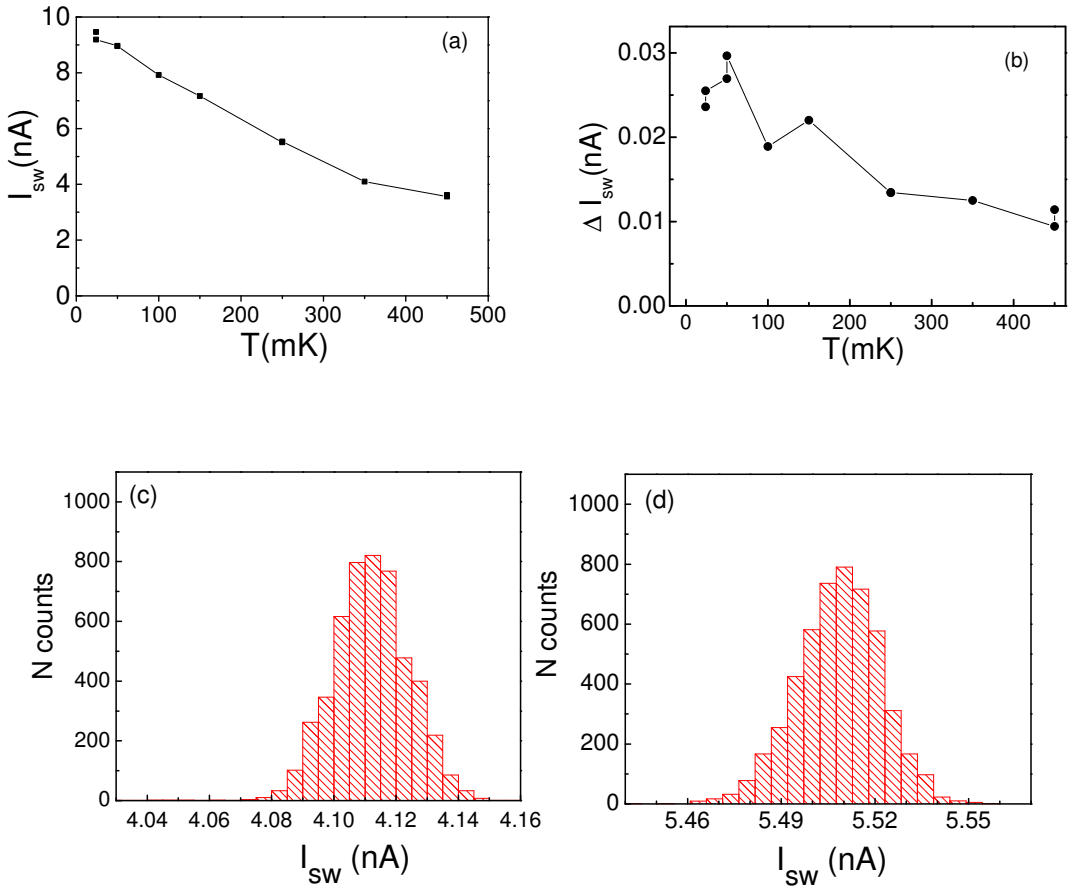

Figure 4.14: Mean switching current (a) and corresponding standard deviation (b) measured at $V_G = -22.3\,\mathrm{V}$ for several temperatures. The histograms measured at T = 350 mK and 250 mK are plotted in (c) and (d).

Chapter 5

Coulomb Blockade

At low temperature and negative gate voltage we found supercurrents for both the nanotube Josephson junctions we measured in a fully filtered dilution refrigerator. At positive values of the gate voltage, on the other hand, Coulomb blockade was observed. In this chapter we present measurements on the Coulomb blockade regime. We recorded the linear conductance as a function of gate and bias voltage in zero and high magnetic field. We observed a quenching of Coulomb blockade in zero field (contacts superconducting) while in high field the diamonds are restored and cotunelling is found. Finally we studied the evolution of the Coulomb peaks in the magnetic field. We found that the levels position shifts and surprisingly some of the peaks split and merge in the magnetic field.

5.1 Coulomb blockade

We now turn the attention to the region at positive gate voltages where Coulomb blockade was found. At low temperature and gate voltgaes, because of the lower transparency of the contacts, single electron charging of the nanotube can be observed[47, 48, 49, 50]. The fingerprint of Coulomb blockade can be seen in the gate dependence of the linear conductance where sharp peaks separated by low conductance regions appear. The exact broadening of the peaks is given by thermal effects in case of small coupling to the contacts while for higher coupling is given by the finite life time of the level. Fig. 5.1 shows the linear conductance measured for our sample at 25 mK in zero magnetic field. For gate voltages $V_G \geq -2\,\mathrm{V}$ we found a large number of regularly spaced Coulomb peaks. The fact that the Coulomb peak spacing does not vary too much over such a broad gate range indicates that the nanotube behaves like a single quantum dot rather than like a series of dots. The latter case is typical of strongly disordered nanotubes where the

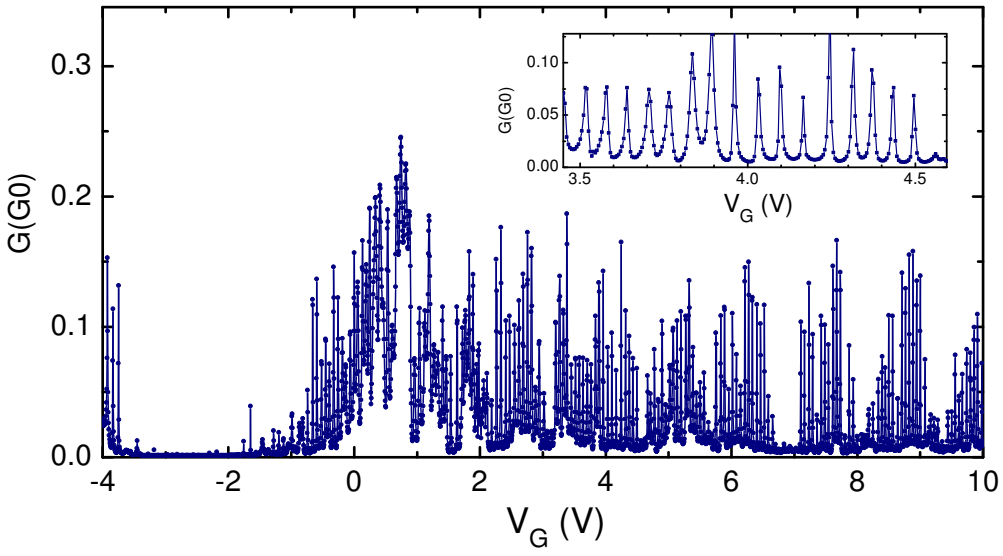

Figure 5.1: Linear conductance measured at 25mK. In the inset a zoom of a few Coulomb peaks. is shown

stability diagram is characterized by a complicated pattern and low conductance at low bias, as shown in Fig.5.2.

For a metallic island with a continuous density of states the gate voltage spacing between the Coulomb peaks is set by the gate capacitance C_G according to the relation:

$$\Delta V_G = e/C_G.$$

When the dimensions of the island are small enough the energy levels become discrete and this is reflected in the peak spacing. Within the constant interaction model the addition energy E_{add}, which is the energy needed to add one electron to the island, is given by the sum of the charging energy E_C and the level spacing δE[3]. In an ideal single wall nanotube the level spacing is related to the distance between the contacts L by the relation $\delta E = hv_F/2L$. For a typical value of $L \approx 350\,\text{nm}$ and $v_F \approx 8 \cdot 10^5 \text{m}^2/\text{s}$ the level spacing is $\delta E \approx 4.7\,\text{eV}$. Each level is then 4 fold degenerate and the linear conductance shows a typical pattern of three equally spaced peaks followed by one with a larger spacing[50]. In multiwall nanotube such a regular pattern is usually not observed,

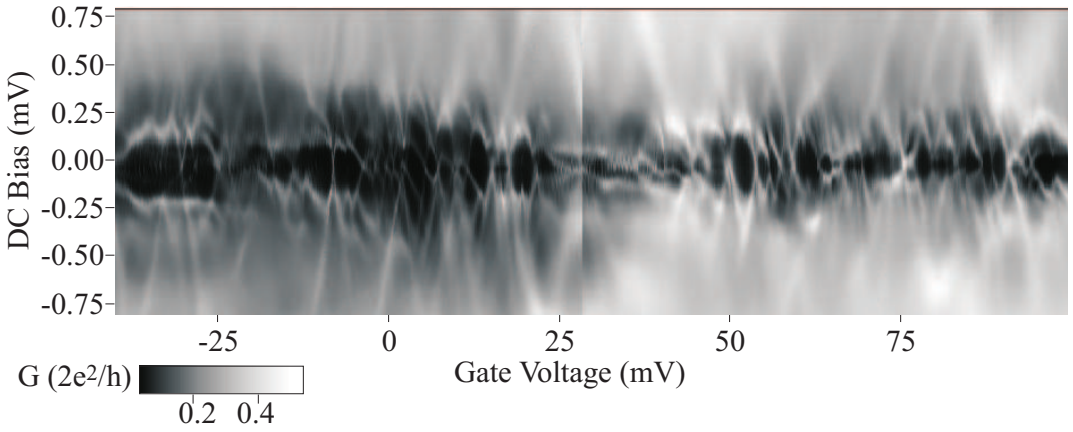

Figure 5.2: Stability diagram of a disordered diffusive multiwall nanotube contacted with gold electrodes and aluminum backgate. The measurements where performed at 25 mK, the Thouless energy of this sample is 70 μeV. Source: B. Stojetz PhD thesis.

and the level spacing found in experiments is much smaller than what one would expect from the contacts spacing L. There are several mechanisms that could be responsible for such a behavior. Due to their larger diameter, multiwall nanotubes have a smaller subband spacing compared to single wall nanotubes so that it is possible that because of intrinsic doping more than just one subband participate in the transport. Moreover in presence of disorder the degeneracy of each level can be lifted. In this case the level distribution would be much more dense than expected for a single wall nanotube. A second possible explanation is that the electrons tunnel into an inner shell and then redistribute over the total length of the nanotube. In this case the level spacing is set by the total length of the nanotube L_{tot} rather than by the contact spacing L[49]. Consequently the level spacing is a factor L_{tot}/L smaller than what extracted from the distance between the contacts L. Even though the level distribution and the dynamics of a complex quantum system such as a multiwall carbon nanotube is clearly an interesting topic, it has not been investigated in details and further studies are desirable. Coulomb blockade measurements allow to probe the level distribution by studying the peak spacing of the linear conductance. In the constant interaction model the two quantities are linked

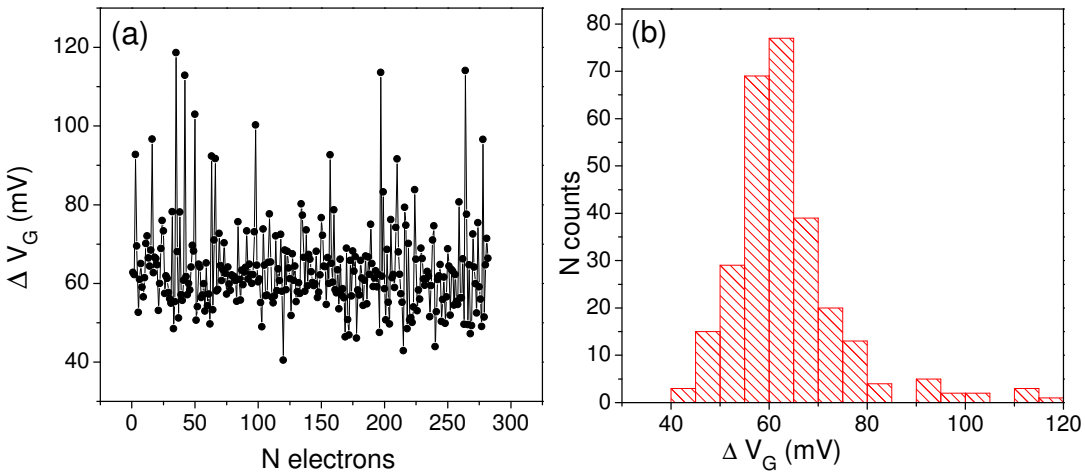

Figure 5.3: (a) Peak spacing versus the number of peaks. We are able to follow the charging of up to about 250 electrons. (b) Histogram of the peak spacing. The shape of the histogram is determined by the transport properties of the dot.

by the following relation[3]:

$$\Delta V_G = \frac{C_\Sigma}{eC_G}\left(e^2/C_\Sigma + \delta E\right) \tag{5.1}$$

with C_Σ the total capacitance of the dot, as defined in Chap. 1.

From a theoretical point of view the level statistics of a mesoscopic system can been studied by using the *random matrix theory* (RMT). This theory has been introduced by Wishart[51] and developed by Wigner[52] in order to explain the excitation energies of nuclei. More recently it has been used to study the peak spacing distribution in semiconducting quantum dots[53, 54, 55, 56, 57]. For a quantum dot with classical chaotic dynamics the RMT predicts a peak spacing that follows a bimodal Wigner--Dyson (WD) distribution for Gaussian orthogonal ensembles. On the other hand, for an integrable system where level repulsion is not present the level spacing is expected to follow a Poissonian distribution. We plot the peak spacing ΔV_G extracted from a single gate sweep in Fig. 5.3. The first graph shows the peak spacing as extracted from the linear conductance. We start counting the peaks from $V_G > -2.5\,\mathrm{V}$, so that $N = 0$

does not correspond to zero electrons in the tube. We estimate that we neglected roughly 20 electrons, assuming that the charge neutrality point is in the middle of the gap region. The right graph shows the corresponding histogram obtained. We compared the measured data with several distributions by estimating the value of two parameters: $\Gamma_1 = \mu_3/\sigma^3$ and $\Gamma_2 = \mu_4/\sigma^4 - 3$, with μ_N the N-th central moment of the peak spacing distribution. We compared these values with predictions of the RMT theory and we found no deviation from a possonian distribution with an average peak spacing of $\Delta V_G = 63$ mV and a standard deviation of about 11 mV. Although this measurements are still preliminary and a more systematic investigation is needed, we note that the Poissonian distribution is unusual and it is generally not observed for quantum dots defined in a two dimensional electron gas.

5.1.1 Stability diagrams

The linear conductance for $V_G \approx -3$ V is extremely low, as it can been seen in Fig. 5.1. We measured the stability diagram in this region and we observed a complex diamond pattern. The maximum differential conductance in this region is about $0.04\ 2e^2/h$. Although the diamonds were sometimes distorted, we could extract an addition energy on the order 3 meV and a gate voltage spacing of the Coulomb peaks of $100-200$ mV. A similar behavior is observed when a magnetic field is applied to suppress superconductivity in the contacts. If the assumption of a semiconducting outermost shell is correct, the charging observed in this gate range corresponds to charging of the inner shell of the tube. Since the stability diagram is very complicated we decided to concentrate our investigations to a region at higher gate voltages where the peaks are more regular and the conductance is higher.

Fig. 5.4 presents the differential conductance as a function of bias and gate voltage, taken at 25 mK for 4.8 V $< V_G <$ 5.7 V. The upper graph was measured with a magnetic field of 6 Tesla applied perpendicular to the substrate, so that the contacts were driven into the normal state. The lower graph refers to measurements in zero field, in this case the niobium contacts are superconducting. The value of the conductance outside the blockade region is rather high for both measurements, and it is on the order of $0.35\ 2e^2/h$. We first analyze the stability diagram in high magnetic field using the simple model presented in Chap.1. We used the diamond pattern to estimate the capacitances of our sample. From the height of the diamonds we extracted an addition energy E_{add} of 1 mV. The lever arm is $\alpha = C_\Sigma/C_G \approx 0.016\ meV/mV$. If we neglect the level spacing, we extract the following values from the slopes of the diamonds: gate

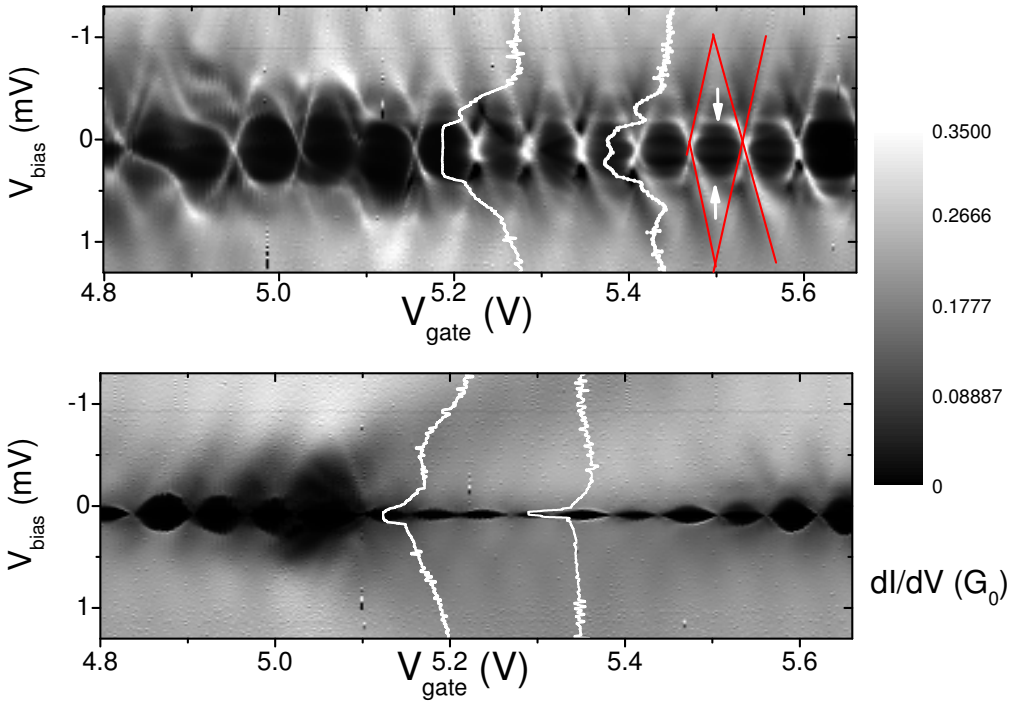

Figure 5.4: Stability diagram measured at 25 mK in 6 Tesla (upper graph) and in 0 magnetic field (lower graph). In high field the contacts are in the normal state and cotunneling is observed as a horizontal ridge of higher conductance at finite bias. We plot two dV/dI traces, in the first we observe cotunneling at finite bias, for the second we observe also a peak at zero bias, that is a signature of the Kondo effect. When the contacts are superconducting it clearly visible that for several diamonds the conductance at low but still finite bias is very high, on the order of 0.3 $2e^2/h$.

capacitance $C_G = 2.5\,\text{aF}$, left and right contact capacitance $C_L \approx C_R \approx 85\,\text{aF}$. The conductance of the sample is not much smaller than the conductance quantum and this indicates a relatively good coupling (for a sample in Coulomb blockade at least) between the nanotube and the contacts. Therefore it can be expected that not only the sequential tunneling is important but also second order processes contribute to the transport [58, 59]. These higher order processes modify the measured stability diagram with respect to what predicted by the orthodox model. The horizontal lines of high conductance inside the diamonds (indicated by white arrows in Fig. 5.4) can be explained by cotunneling, a second order process that involves the simultaneous tunneling of two electrons [60]. We also found that for certain diamonds the differential conductance has a peak at zero bias which is typical signature of the Kondo effect [58]. When the magnetic field is turned off the contacts are superconducting and the stability diagram is strongly modified. The measurements in zero and in high magnetic field seem to be shifted with respect to gate voltage of about $60\,\text{mV}$. The evolution of the levels position in a magnetic field will be analyzed in the next section. The main feature of the stability diagram is a strong suppression of Coulomb blockade for several diamonds over a broad gate voltage range. The spacing of the Coulomb peaks is unchanged, which seems to exclude that the addition energy is changed, but the conductance inside the diamonds is much higher with the contacts superconducting rather than normal. Although we don not have a conclusive explanation for this effect we suggest that Andreev processes at intermediate transparency could enhance the cotunelling and therefore suppress the blockade at finite bias. Fig.5.4 shows the line scans for two gate voltages at 0 and 6 Tesla (the gate voltage at which the line scans are taken are shifted to try to compensate the effect of the magnetic field on the level position). The comparison between the line scans at 0 and 6 Tesla magnetic field suggests a correlation between the cotunneling and the suppression of the Coulomb blockade. The Coulomb blockade is suppressed at lower bias voltage for those diamonds where also the cotunneling becomes effective at lower bias.

5.1.2 Magnetic field dependence

The qualitative behavior observed in the measurements presented in the previous section has been reproduced for several gate voltages and in different cooldowns. The stability diagram measured at zero magnetic field for the gate range $-4\ \text{V} < V_G < -3\ \text{V}$ is presented in Fig. 5.5. The average peak spacing is approximatively the same as in the previous cooldown and we found again that Coulomb blockade is suppressed at finite

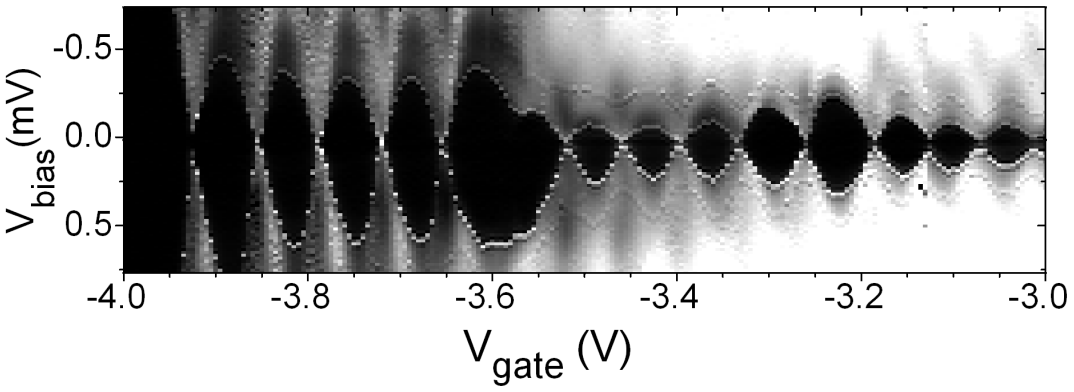

Figure 5.5: Stability diagram measured in zero field at 50 mK in a second cooldown, white correspond to a differential conductance of $0.4 \cdot 2e^2/h$. The contacts are in the superconducting state and for $V_G > -3.5$ V the blockade is quenched. The quenching is not always symmetric with respect to the applied bias voltage.

bias for several gate voltages. For some of the diamonds, the suppression is asymmetric with respect to the bias voltage.

When a magnetic field is applied perpendicular to the sample the energy levels of the tube are changed due to Zeeman and orbital effects. The shift of the energy levels can be studied by measuring the linear conductance as a function of magnetic field and looking at the variation of the peak positions. The magnetic field reduces also the gap of the superconducting contacts. The critical field of the contacts is $B_c \approx 3$ T, for higher values of B the contacts are not superconducting.

We plot the linear conductance as a function of gate voltage and magnetic field in Fig. 5.6. Black corresponds to zero conductance and white indicates higher conductance, so that the (almost) horizontal white lines on the 2D plot contain information about the shift of the level position in a magnetic field. Indeed the lines are not exactly horizontal but they have a finite slope. The slope changes for different peaks and even for a single peak it can change for different ranges of the magnetic field. In semiconducting quantum dots this is usually associated with a transition from one state to an other with different angular momentum or spin. We used the lever arm extracted from the Coulomb blockade measurements to translate the gate voltage shift into the corresponding energy shift and

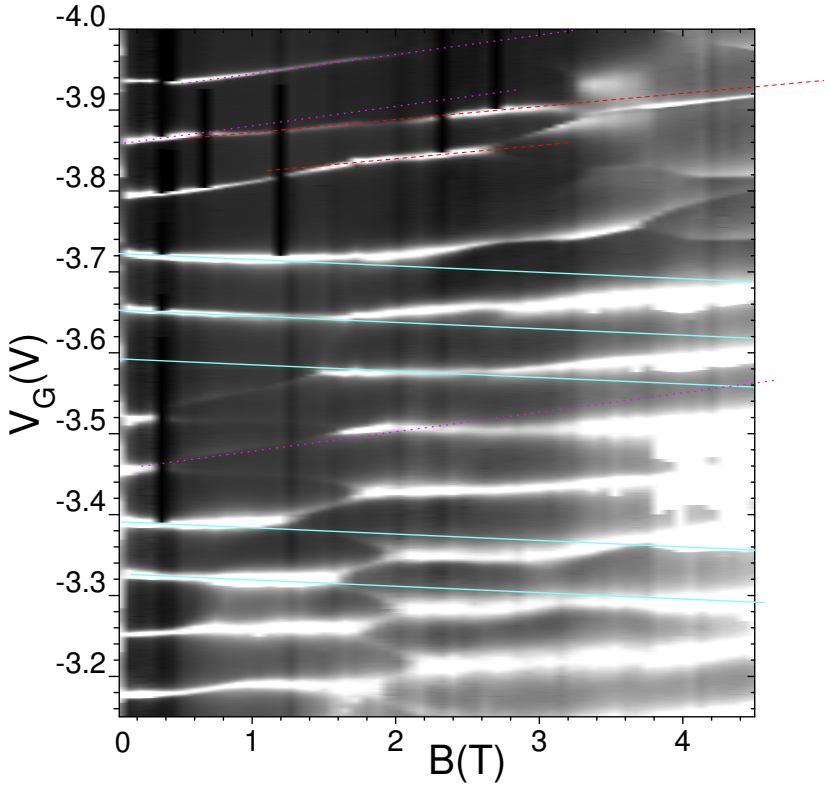

Figure 5.6: Magnetic field dependence of the level positions. The corresponding stability diagram in zero field is shown in Fig. 5.5. The lines represent a slope of $\Delta V_G/T = A \cdot g\mu_B/\alpha$, with $A = 1, 2, 3$.

vice versa. The blue line in the plot shows the level shift due to Zeeman. The slope is given by $\Delta V_G/T = g\mu_B/\alpha = 2 \cdot 0.56/0.016\,\mathrm{mV/T} \approx 7\,\mathrm{mV/T}$. The other lines are obtained by multipling the slope of the blue line by a factor 2 and 3. We found that groups of peaks share the same approximative slope.

The most striking feature of the measurement is that some of the peaks splits when the magnetic field is applied and eventually, if the field is increased further, these split peaks merge again. The conductance of the split peaks is strongly reduced, typically by a factor between 10-100 compared to the unsplit peak. Interestingly, the position of the split Coulomb peaks show a stronger B dependence with respect to the unsplit peaks. An explanation for this behavior, observed also for other gate ranges, is still missing. A

similiar effect has been reported in quantum dots where charge traps where fabricated into the tunnel barriers [61]. For such a system the splitting of the peak corresponds to a charging of the trap. Whether a similar model can be applyied to our multiwall nanotube, where for instance an inner shell acts as a charge trap rather than an impurity into the barrier, is still unclear.

Magnetic field dependence in the ^{3}He-cryostat

In this section we report a similar measurement on a third cooldown, performed this time in our ^{3}He-cryostat three cryostat at 360 mK. The measurements show again a suppression of the Coulomb blockade in zero field, as it can be seen in Fig.5.7. The line scans for two gate voltages at zero and 5 Tesla are also shown. At $B = 5\,\mathrm{T}$ well above B_C of niobium, the Coulomb diamonds are restored, even though this time the measurements are more noisy compared to the first cooldown. We measured the linear conductance as a function of the magnetic field up to 8 Tesla. At low field the measurements are similar to those reported in the previous section, and lines with a well defined slopes are visible. At high fields the magnetic field dependence is more strong probably due to orbital effects and the pattern becomes very complicated. The measurements are presented in Fig.5.8. A similar pattern at high field was obtained for a second gate region (not shown). Fig.5.8 (b) shows a zoom of the gate range around $V_G \approx 1.8\,V$ for $0\,\mathrm{T} < B < 1.5\,\mathrm{T}$. The red lines are meant as a guide to the eyes. As for the measurements presented in the previous section, we find that several consecutive peaks shift with the same slope in the magnetic field. While some of the peaks are almost horizontal, two couple of peaks shift in opposite way in the magnetic field with a measurable slope. For this two groups of peak the observed slope is on the order of 30 mV/T, much bigger than what expected of from Zeeman splitting of only about 7 mV/T, and indicates that orbital effects are strong in our sample.

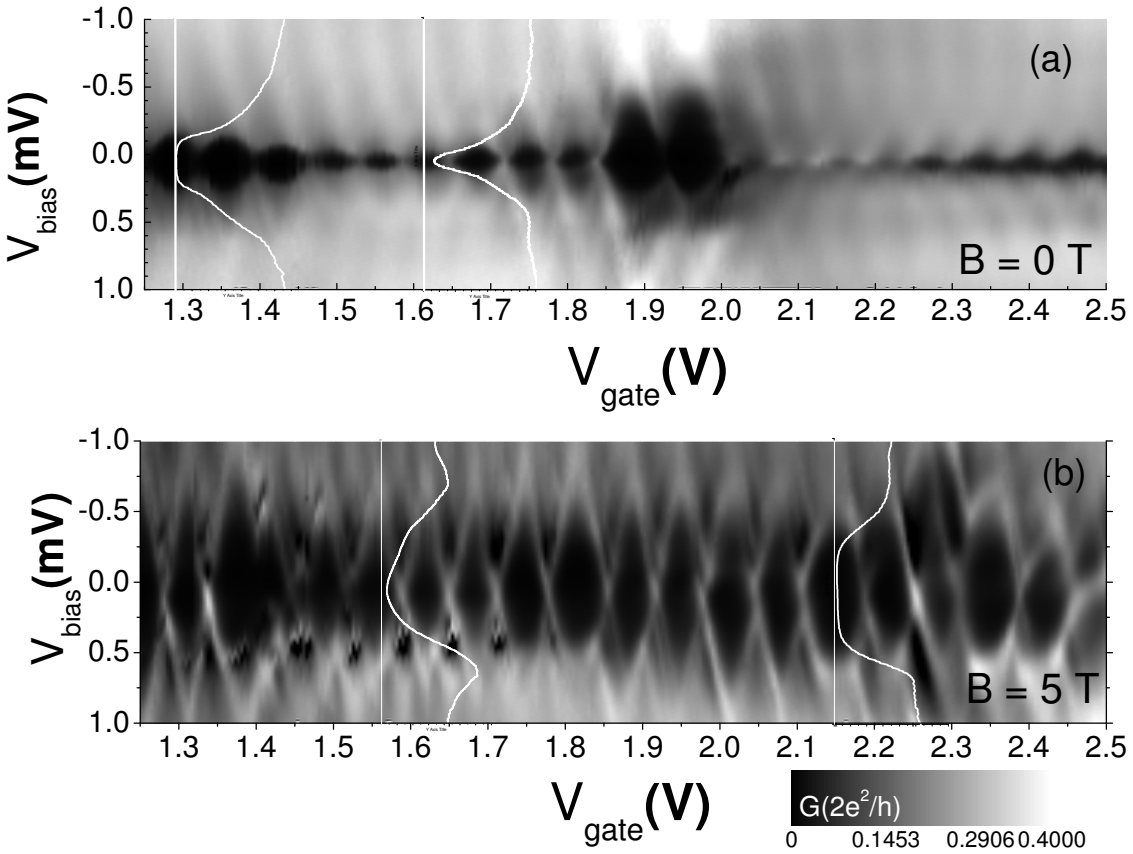

Figure 5.7: Coulomb blockade measured at 360 mK. We observed the same behavior as in the other cooldowns with suppressed blockade at zero field (b). The diamonds in high magnetic field (a) have approximately the same dimensions than in the previous measurements.

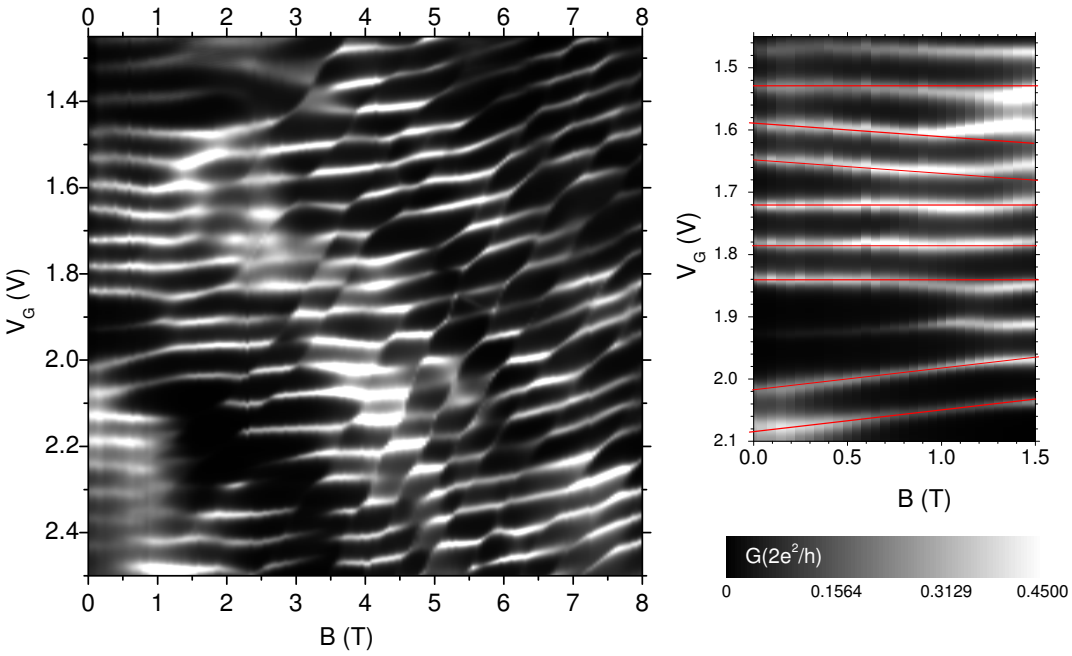

Figure 5.8: Linear conductance as a function of the magnetic field. The corresponding stability diagram in zero and high magnetic field is shown in Fig. 5.7. On the right graph we present a zoom of the measurements at low field. The position of some of the peaks is almost insensitive to magnetic field while other peaks are strongly shifted when magnetic field is applied.

Chapter 6

Summary

The main focus of this work has been the experimental investigation of multiwall carbon nanotubes connected to superconducting leads made of niobium. The samples have been prepared by contacting individual nanotubes dispersed onto an oxidized silicon substrate.The electromagnetic environment into which the junction is embedded is formed by lithographically defined on chip resistors and capacitors and has been optimized to reduce the suppression of supercurrent due to thermal fluctuations. The transport through such a junction has been investigated at very low temperatures. We found supercurrents that are high compared to previous reports in gated nanotubes. The maximum value of the measurable supercurrent, the switching current, is found to have a resonant-like behavior as a function of gate voltage and a strong temperature dependence. We used the extended RCSJ model to analyze the switching of the junction. The model correctly predicts the hysteretic behavior of the IV characteristic observed in the measurements and reproduces the measured switching and retrapping currents over a wide temperature range using only one free parameter, the critical current of the junction. The comparison between the effects of temperature and magnetic field on the retrapping current supports our interpretation. The ratio between the intrinsic critical current and the measured switching current is only a factor of two. This low value is due to the properly designed electromagnetic environment. The small critical current Josephson junctions are very sensitive to external noise so that the effective electron temperature can be much higher than the bath temperature. In our measurements the good agreement between the measured data and the theoretical prediction for temperatures above 50 mK indicates that the switching is mainly due to thermal fluctuations rather than electromagnetic noise. By comparing the shape of the supercurrent resonance and the conductance in the resistive branch as a function of gate voltage we conclude that the junctions behave like an open

quantum, similarly to what is observed for single wall nanotubes.
We note that the determination of the critical current from the temperature dependence of the measured switching currents is a key ingredient for any comparison between theory and experiments and applies to single wall carbon nanotube as well. It would certainly be interesting to repeat the experiments presented in this work with a single wall nanotube which is a system that is easier to characterize and combine the physics of one-dimensional system with that of strong electron-electron interactions.
At positive gate voltages we found Coulomb blockade. From the linear conductance we extract the peak spacing and we fit it with a Poissonian distribution. The stability diagrams in zero field and high magnetic field are also measured.
At intermediate conductance cotunneling is observed when the contacts are in the normal state. On the other hand, when the contacts are in the superconducting state the blockade is quenched at finite bias. Finally we investigated the magnetic field dependence of the linear conductance and found that surprisingly several Coulomb peaks split and merge in the magnetic field. This effect is observed in several gate regions and for different cooldowns. The regularity of the measurements in the Coulomb blockade regime allows to further characterize the multiwall carbon nanotube and confirms that our nanotube junctions behave like a single quantum dot.

Appendix A

Recipe

1. Alignment marks are patterned with standard electron beam lithography on a strongly doped silicon substrate with 400 nm thermal oxide.
2. Evaporation of chromium (5 nm) gold (80 nm) in a HV chamber.
3. Lift-off with hot acetone.
4. Deposition of a droplet of suspension of multiwall carbon nanotube dispersed in 1,2 Dichlorethanol on top of the sample. After several minutes the droplet is washed away with propanol.
5. The MWNT are located by means of scanning electron microscopy.
6. Preparation of the leads.
    - EBL Resist: PMMA 200K 7%, Dose: 280 μC/cm^2, development: propanol/MLBK (3:1) for 3 minutes + 30 sec. propanol
    - Evaporation of titanium (5 nm) and a palladium-gold alloy (55 nm).
    - Lift-off in hot acetone, 60 degree.
7. Preparation of the contacts.
    - EBL Resist: PMMA 200K 3,5%, Dose: 350 μC/cm^2, development: MLBK for 30 sec. + 30 sec. Propanol.
    - Evaporation of 3 nm of palladium in UHV.
    - In the same vacuum run, sputtering of 45 nm of niobium.
    - Lift-off in hot acetone.

Appendix B

Filtering Scheme

Our dilution refrigerator is mounted in a shielded box which each line enters through a π with a cutoff frequency of about 100 MHz. A second room temperature π filter stage is installed at the top of the cryostat and two copper powder filter stages (cutoff at about 300 MHz) are mounted at the 1 K and the 100 mK plate, as shown Fig.B.1. These filters provide a very efficient thermalization of the line and keep the electron temperature as close as possible to the bath temperature by filtering out the hot photons of the blackbody radiation of the cryostat's parts at the 4.2 K. For this experiment we mounted one extra low temperature RC filtering stage. This stage is used to reduce the noise at low frequency that is very effectively in suppressing the supercurrent in small Josephson junctions. The circuit scheme is taken from the supplementary information of ref. [38]. This two stage RC filter is characterized by a damping of 40dB/Octave with a cutoff frequency of about 10 KHz. Fig.B.1 shows the circuit diagram and four RC filters:

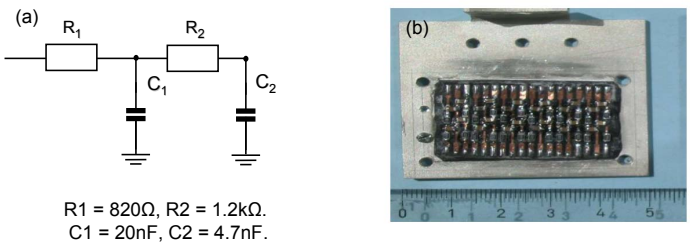

Figure B.1: Schematic of the two stage RC filters. Silver platine with 4 RC filters.

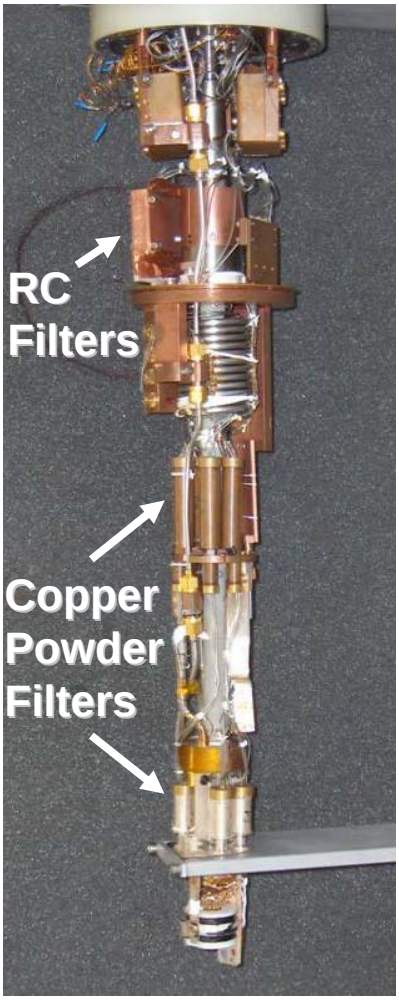

Figure B.2: Lower part of the insert of our dilution refrigerator. The low temperature filtering stages are indicated.

Bibliography

[1] R. Saito and M. Dresselhaus. *Physical properties of carbon nanotubes*.

[2] Jean C. Charlier, Xavier Blase, and Stephan Roche. Electronic and transport properties of nanotubes. *Reviews of Modern Physics*, 79(2), 2007.

[3] P. L. McEuen S. Tarucha R. M. Westervelt S. Wingreen Leo P. Kouwenhoven, C. M. Marcus. Electron transport in quantum dots. *Mesoscopic Electron Transport*.

[4] M. Walliser. *PhD Thesis*. 2002.

[5] T. Nakanishi T. Ando and R. Saito. Berrys's phase and absence of back scattering in carbon nanotubes. *J. Phys. Soc. Jpn.*, 67, 1998.

[6] Bernard Stojetz, Csilla Miko, Laszlo Forro, and Christoph Strunk. Effect of band structure on quantum interference in multiwall carbon nanotubes. *Physical Review Letters*, 94(18):186802, 2005.

[7] B. Bourlon, C. Miko, L. Forró, D. C. Glattli, and A. Bachtold. Determination of the intershell conductance in multiwalled carbon nanotubes. *Phys. Rev. Lett.*, 93(17):176806, Oct 2004.

[8] Shidong Wang and Milena Grifoni. Transport properties of double-walled carbon nanotube quantum dots. *Physical Review B (Condensed Matter and Materials Physics)*, 77(8):085431, 2008.

[9] Jia Lu Andrew G. Rinzler Richard E. Smalley Leon Balents Marc Bockrath, David H. Cobden and Paul L. McEuen. Luttinger-liquid behaviour in carbon nanotubes. *Nature*, 397, 1999.

[10] Dolores Bozovic Jason H. Hafner M. Tinkham Hongkun Park Wenjie Liang, Marc Bockrath. Fabry - perot interference in a nanotube electron waveguide. *Nature*, 411, 2001.

[11] Herre S.J. van der Zant Cees Dekker Leo P. Kouwenhoven Silvano De Franceschi Pablo Jarillo-Herrero, Jing Kong. Orbital kondo effect in carbon nanotubes. *Nature*, 434, 2005.

[12] P. Woelfle N. Mason C. M. Marcus J. Nygard J. Paaske, A. Rosch. Non-equilibrium singlet triplet kondo effect in carbon nanotubes. *Nature Physics*, 2, 2006.

[13] Marc Bockrath Vikram V. Deshpande. The one-dimensional wigner crystal in carbon nanotubes. *Nature Physics*, 4, 2008.

[14] S. Datta. *Electronic Transport in Mesoscopic System*.

[15] B. L. Altshuler and A. G. Aronov. *JETP*, 33, 1981.

[16] C. W. J. Beenakker and H. van Houten. Flux-cancellation effect on narrow-channel magnetoresistance fluctuations. *Phys. Rev. B*, 37(11):6544–6546, Apr 1988.

[17] M. Tinkham. *Introduction to superconductivity*. McGraw-Hill, New York, 1975.

[18] R. Kleiner W. Buckel. *Supraleitung: Grundlagen und Anwendungen*. Wiley-VCH, Weinheim, 2004.

[19] J. M. Martinis and R. L. Kautz. Classical phase diffusion in small hysteretic josephson junctions. *Phys. Rev. Lett.*, 63(14):1507–1510, Oct 1989.

[20] R. L. Kautz and John M. Martinis. Noise-affected i-v curves in small hysteretic josephson junctions. *Phys. Rev. B*, 42(16):9903–9937, Dec 1990.

[21] H. Kamerlingh Onnes. *Leiden Comm.*, 120, 1911.

[22] B. D. Josephson. Possible new effects in superconductive tunnelling. *Physics Letters*, 1:251–253, July 1962.

[23] B. D. Josephson. The discovery of tunnelling supercurrents. *Rev. Mod. Phys.*, 46(2):251–254, Apr 1974.

[24] K. K. Likharev. Superconducting weak links. *Rev. Mod. Phys.*, 51(1):101–159, Jan 1979.

[25] M. F. Goffman, R. Cron, A. Levy Yeyati, P. Joyez, M. H. Devoret, D. Esteve, and C. Urbina. Supercurrent in atomic point contacts and andreev states. *Phys. Rev. Lett.*, 85(1):170–173, Jul 2000.

[26] P. Dubos, H. Courtois, B. Pannetier, F. K. Wilhelm, A. D. Zaikin, and G. Schön. Josephson critical current in a long mesoscopic s-n-s junction. *Phys. Rev. B*, 63(6):064502, Jan 2001.

[27] V. Ambegaokar and A. Baratoff. Tunneling between superconductors. *Phys. Rev. Lett.*, 10(11):486–489, Jun 1963.

[28] I. O. Kulik and A. N. Omelyanchuk. Contribution to the microscopic theory of the josephson effect in superconducting bridges. *JETP Lett.*, 21:96–97, 1975.

[29] G. F. Zharkov A. D. Zaikin. *Sov. J. Low Temp. Phys.*, 7, 1981.

[30] C. W. J. Beenakker and H. van Houten. Josephson current through a superconducting quantum point contact shorter than the coherence length. *Phys. Rev. Lett.*, 66(23):3056–3059, Jun 1991.

[31] A. Franz, Y. Koval, D. Vasyukov, P. Müller, H. Schneidewind, D. A. Ryndyk, J. Keller, and C. Helm. Thermal fluctuations in ultrasmall intrinsic josephson junctions. *Phys. Rev. B*, 69(1):014506, Jan 2004.

[32] D. Ryndyk. Thermal fluctuations and premature switching of josephson junctions. *Unpublished*.

[33] T. Kontos. *PhD Thesis*. 2002.

[34] Qian Wang Mark Lundstrom Ali Javey, Jing Guo and Hongjie Dai1. Ballistic carbon nanotube field-effect transistors. *Nature*, 424, 2003.

[35] Norbert Nemec, David Tomanek, and Gianaurelio Cuniberti. Contact dependence of carrier injection in carbon nanotubes: An ab initio study. *Physical Review Letters*, 96(7):076802, 2006.

[36] A. Makarovski, J. Liu, and G. Finkelstein. Evolution of transport regimes in carbon nanotube quantum dots. *Physical Review Letters*, 99(6):066801, 2007.

[37] P.E. Lindelof K. Groove-Rasmussen, H.I. Jorgensen. *Physica E*, 2007.

[38] Jorden A. van Dam Pablo Jarillo-Herrero and Leo P. Kouwenhoven. Quantum supercurrent transistors in carbon nanotubes. *Nature*, 439, 2006.

[39] J. P. Cleuziou, W. Wernsdorfer, V. Bouchiat, Th. Ondarcuhu, and M. Monthioux. Carbon nanotube superconducting quantum interference device. 2006.

[40] T. Tsuneta, L. Lechner, and P. J. Hakonen. Gate-controlled superconductivity in a diffusive multiwalled carbon nanotube. *Physical Review Letters*, 98(8):087002, 2007.

[41] M. Kociak B. Reulet H. Bouchiat I. I. Khodos Yu. B. Gorbatov V. T. Volkov C. Journet A. Yu. Kasumov, R. Deblock and M. Burghard. Supercurrents through single-walled carbon nanotubes. *Science*, 28, 1999.

[42] M. Weiss C. Karrasch V. Meden C. Schonenberger H. Bouchiat A. Eichler, R. Deblock. Tuning the josephson current in carbon nanotubes with the kondo effect. *arXiv:0810.1671v1*, 2008.

[43] K. Grove-Rasmussen K. Flensberg P. E. Lindelof. H. I. Jorgensen, T Novotny. Critical current 0-pi transition in designed josephson quantum dot junctions. *Nano letters*, 7(8), 2007.

[44] b C. W. J. Beenakkera and H. van Houtena. Resonant josephson current through a quantum dot. *Single-Electron Tunneling and Mesoscopic Devices*.

[45] Artem V. Galaktionov and Andrei D. Zaikin. Quantum interference and supercurrent in multiple-barrier proximity structures. *Phys. Rev. B*, 65(18):184507, Apr 2002.

[46] Grygoriy Tkachov and Klaus Richter. Effect of magnetic pair breaking on andreev bound states and resonant supercurrent in quantum dot josephson junctions. *Physical Review B (Condensed Matter and Materials Physics)*, 75(13):134517, 2007.

[47] H. Dai A. Thess-R.E. Smalley L.J. Geerligs C. Dekker S.Tans, M.H. Devoret. Individual single-wall nanotubes as. quantum wires. *Nature*, 386, 1997.

[48] Z. Yao M. Grifoni C. Dekker H.W.Ch. Postma, T.F. Teepen. Carbon nanotubes single-electron transistors at room temperature. *Nature*, 293, 2001.

[49] M. R. Buitelaar, A. Bachtold, T. Nussbaumer, M. Iqbal, and C. Schönenberger. Multiwall carbon nanotubes as quantum dots. *Phys. Rev. Lett.*, 88(15):156801, Mar 2002.

[50] L. Kouwenhoven H.S. van der Zant P.J. Herrero, S. Sampaz. Electron-hole symmetry in a semiconducting carbon nanotube quantum dot. *Nature*, 429, 2004.

[51] J. Wishart. Generalized product moment distribution in samples. *Biometrika A*, 20, 1928.

[52] E.P. Wigner. On the statistical distribution of the widths and spacings of nuclear resonance levels. *Proc. Camb. Phil. Soc.*, 47, 1955.

[53] Dyson. Statistical theory of the energy levels of complex systems. *J. Math. Phys.*, 3, 1962.

[54] C. W.!Beenakker. Random-matrix theory of quantum transport. *Rev. Mod.Phys.*, 69, 1997.

[55] A. M. Chang, H. U. Baranger, L. N. Pfeiffer, K. W. West, and T. Y. Chang. Non-gaussian distribution of coulomb blockade peak heights in quantum dots. *Phys. Rev. Lett.*, 76(10):1695–1698, Mar 1996.

[56] J. A. Folk, S. R. Patel, S. F. Godijn, A. G. Huibers, S. M. Cronenwett, C. M. Marcus, K. Campman, and A. C. Gossard. Statistics and parametric correlations of coulomb blockade peak fluctuations in quantum dots. *Phys. Rev. Lett.*, 76(10):1699–1702, Mar 1996.

[57] M. Boehm, M. Hofheinz, X. Jehl, M. Sanquer, M. Vinet, B. Previtali, D. Fraboulet, D. Mariolle, and S. Deleonibus. Size scaling of the addition spectra in silicon quantum dots. *Physical Review B (Condensed Matter and Materials Physics)*, 71(3):033305, 2005.

[58] P. E. Lindelof J. Nygard, D. H. Cobden. Kondo physics in carbon nanotubes. *Nature*, 408, 2000.

[59] B. Babić and C. Schönenberger. Observation of fano resonances in single-wall carbon nanotubes. *Phys. Rev. B*, 70(19):195408, Nov 2004.

[60] S. De Franceschi, S. Sasaki, J. M. Elzerman, W. G. van der Wiel, S. Tarucha, and L. P. Kouwenhoven. Electron cotunneling in a semiconductor quantum dot. *Phys. Rev. Lett.*, 86(5):878–881, Jan 2001.

[61] M. Hofheinz. Phd thesis. *Unpublished, http://tel.archives-ouvertes.fr/tel-00131052/en/*, 2006.

Acknowledgements

First of all, I wish to thank my supervisor Prof. Strunk. I admire your way of understanding the physics, I am glad I had the chance to work for and with you. Physics can be frustrating, your support has been important on this regard as well.

Prof. Forro provided the outstanding nanotubes that have been used for this thesis. A special thank goes to Dr. Ryndyk, your collaboration has been fundamental for the success of this thesis. I would also like to thank Dr. Adagideli and Dr. Rycerz for the discussions concerning the level statistics. I'm in debt with Martin and Tom, our great technicians, the all Lehrstuhl of Prof. Weiss and to all the electronics workshop. As low temperature experimentalist I cannot forget the "Helium guys" that provided ne with liquid helium. I'm grateful to Dr. Eroms and all the others that read this manuscript, your suggestions have been invaluable.

I would like to thank all the colleagues, postdocs, students and guests that I had the pleasure to work with, those who left and those who will stay, with a special thank to all my former office mates! I learned much from you all, and I miss already the magic atmosphere of our group and its internationality. A special good luck to the new "generation" David, Lorenz, Wolfgang, Matthias and Markus II.

Grazie alla mia famiglia, che ha supportato la mia decisione di andare lontano per il solo fatto che fosse quello che io volessi. Babbo, mamma, grazie per tutti i sacrifici che avete fatto per dare la possibilita' di studiare a tutti e tre i vostri bambini. Cari Leo e Fede, mi siete mancati ma non vi ho mai sentito veramente lontani, sopratutto te Leo, sai quanto questo sia importante quando si e' lontani da casa. Sorellina, ricordati che ci sono sempre se tu dovessi avere bisogno, a Parigi come a Regensburg.

Tom, Markus, Dominik, Andi, Flo, you have been by far more than just coworkers. I consider you together with Nici, Beate, Aina, Agnes, Ben, Susanne, Scott, Tenorman, and Andi very good friends. It is because of you that I felt home at Regensburg. Yes, from time to time (very rarely I'd say) I may have been complaining a bit because of the weather or the food, but you know how much I loved to stay in Regensburg. Thanks for

letting me feel like one of you and not only the Italian PhD student (still I have to say that lunch at 11.30 cannot be right ;). Gernot, I will miss you and our usual beers at number 7, I'm sure we will see soon!
Francesco, Christoph, Michael, our evenings spent talking and playing Schapkopf while learning German have been just fantastic. Giovanni, Pasquale, Karolina, Dario, Manuela, Pino, Giuseppe, Fabio-sihhe', Silvia, you brought a bit of the Italian sunshine in Germany. And great thanks to the all the friends that I left in Italy, the Gruppospacca and all the gang of Rifredi!
Giulia, my love. It is always hard to leave, and it has been hard to leave Regensburg. But when leaving I knew that there is so much we want to see, so many things we want to do that was just right to move on. Now, I'm almost ready to start again, newly. I was still waiting for you, because this time we could have done it together, as I wanted so much.